A measurement of the Tau topological branching ratios

The DELPHI Collaboration

P. Abreu[23], W. Adam[52], T. Adye[38], P. Adzic[12], Z. Albrecht[19], T. Alderweireld[2], G.D. Alekseev[18], R. Alemany[9],
T. Allmendinger[19], P.P. Allport[24], S. Almehed[26], U. Amaldi[30], N. Amapane[47], S. Amato[49], E. Anashkin[37],
E.G. Anassontzis[3], P. Andersson[46], A. Andreazza[29], S. Andringa[23], N. Anjos[23], P. Antilogus[27], W-D. Apel[19],
Y. Arnoud[16], B. Åsman[46], J-E. Augustin[25], A. Augustinus[9], P. Baillon[9], A. Ballestrero[47], P. Bambade[21], F. Barao[23],
G. Barbiellini[48], R. Barbier[27], D.Y. Bardin[18], G. Barker[19], A. Baroncelli[40], M. Battaglia[17], M. Baubillier[25],
K-H. Becks[54], M. Begalli[6], A. Behrmann[54], T. Bellunato[9], Yu. Belokopytov[9], K. Belous[44], N.C. Benekos[33],
A.C. Benvenuti[5], C. Berat[16], M. Berggren[25], L. Berntzon[46], D. Bertrand[2], M. Besancon[41], N. Besson[41], M.S. Bilenky[18],
D. Bloch[10], H.M. Blom[32], J. Bol[19], M. Bonesini[30], M. Boonekamp[41], P.S.L. Booth[24], G. Borisov[21], C. Bosio[43],
O. Botner[50], E. Boudinov[32], B. Bouquet[21], T.J.V. Bowcock[24], I. Boyko[18], I. Bozovic[12], M. Bozzo[15], M. Bracko[45],
P. Branchini[40], R.A. Brenner[50], E. Brodet[36], P. Bruckman[9], J-M. Brunet[8], L. Bugge[34], P. Buschmann[54], M. Caccia[29],
M. Calvi[30], T. Camporesi[9], V. Canale[39], F. Carena[9], L. Carroll[24], C. Caso[15], A. Cattai[9], F.R. Cavallo[5], M. Chapkin[44],
Ph. Charpentier[9], P. Checchia[37], G.A. Chelkov[18], R. Chierici[9], P. Chliapnikov[9,44], P. Chochula[7], V. Chorowicz[27],
J. Chudoba[31], S.H. Chung[9], K. Cieslik[20], P. Collins[9], R. Contri[15], G. Cosme[21], F. Cossutti[9], M. Costa[51], H.B. Crawley[1],
D. Crennell[38], J. Croix[10], J. Cuevas Maestro[35], S. Czellar[17], J. D'Hondt[2], J. Dalmau[46], M. Davenport[9], W. Da Silva[25],
G. Della Ricca[48], P. Delpierre[28], N. Demaria[47], A. De Angelis[48], W. De Boer[19], C. De Clercq[2], B. De Lotto[48],
A. De Min[37], L. De Paula[49], H. Dijkstra[9], L. Di Ciaccio[39], K. Doroba[53], M. Dracos[10], J. Drees[54], M. Dris[33],
G. Eigen[4], T. Ekelof[50], M. Ellert[50], M. Elsing[9], J-P. Engel[10], M. Espirito Santo[9], G. Fanourakis[12], D. Fassouliotis[12],
M. Feindt[19], J. Fernandez[42], A. Ferrer[51], E. Ferrer-Ribas[21], F. Ferro[15], A. Firestone[1], U. Flagmeyer[54], H. Foeth[9],
E. Fokitis[33], F. Fontanelli[15], B. Franek[38], A.G. Frodesen[4], R. Fruhwirth[52], F. Fulda-Quenzer[21], J. Fuster[51],
D. Gamba[47], S. Gamblin[21], M. Gandelman[49], C. Garcia[51], C. Gaspar[9], M. Gaspar[49], U. Gasparini[37], Ph. Gavillet[9],
E.N. Gazis[33], D. Gele[10], T. Geralis[12], N. Ghodbane[27], F. Glege[54], R. Gokieli[9,53], B. Golob[45], G. Gomez-Ceballos[42],
P. Goncalves[23], I. Gonzalez Caballero[42], G. Gopal[38], L. Gorn[1], Yu. Gouz[44], V. Gracco[15], J. Grahl[1], E. Graziani[40],
G. Grosdidier[21], K. Grzelak[53], J. Guy[38], C. Haag[19], F. Hahn[9], S. Hahn[54], S. Haider[9], Z. Hajduk[20], A. Hallgren[50],
K. Hamacher[54], K. Hamilton[36], J. Hansen[34], F.J. Harris[36], S. Haug[34], F. Hauler[19], V. Hedberg[9,26], S. Heising[19],
P. Herquet[2], H. Herr[9], O. Hertz[19], E. Higon[51], S-O. Holmgren[46], P.J. Holt[36], S. Hoorelbeke[2], M. Houlden[24],
J. Hrubec[52], G.J. Hughes[24], K. Hultqvist[9,46], J.N. Jackson[24], R. Jacobsson[9], Ch. Jarlskog[26], G. Jarlskog[26], P. Jarry[41],
B. Jean-Marie[21], D. Jeans[36], E.K. Johansson[46], P. Jonsson[27], C. Joram[9], P. Juillot[10], L. Jungermann[19], F. Kapusta[25],
K. Karafasoulis[12], S. Katsanevas[27], E.C. Katsoufis[33], R. Keranen[19], G. Kernel[45], B.P. Kersevan[45], B.A. Khomenko[18],
N.N. Khovanski[18], A. Kiiskinen[17], B. King[24], A. Kinvig[24], N.J. Kjaer[9], O. Klapp[54], P. Kluit[32], P. Kokkinias[12],
V. Kostioukhine[44], C. Kourkoumelis[3], O. Kouznetsov[18], M. Krammer[52], E. Kriznic[45], Z. Krumstein[18], P. Kubinec[7],
W. Kucewicz[20], M. Kucharczyk[20], J. Kurowska[53], J.W. Lamsa[1], J-P. Laugier[41], G. Leder[52], F. Ledroit[16], L. Leinonen[46],
A. Leisos[12], R. Leitner[31], J. Lemonne[2], G. Lenzen[54], V. Lepeltier[21], M. Lethuillier[27], J. Libby[9], W. Liebig[54], D. Liko[9],
A. Lipniacka[46], I. Lippi[37], J.G. Loken[36], J.H. Lopes[49], J.M. Lopez[42], R. Lopez-Fernandez[16], D. Loukas[12], P. Lutz[41],
L. Lyons[36], J. MacNaughton[52], J.R. Mahon[6], A. Maio[23], A. Malek[54], S. Maltezos[33], V. Malychev[18], F. Mandl[52],
J. Marco[42], R. Marco[42], B. Marechal[49], M. Margoni[37], J-C. Marin[9], C. Mariotti[9], A. Markou[12], C. Martinez-
Rivero[9], S. Marti i Garcia[9], J. Masik[13], N. Mastroyiannopoulos[12], F. Matorras[42], C. Matteuzzi[30], G. Matthiae[39],
F. Mazzucato[37,14], M. Mazzucato[37], M. Mc Cubbin[24], R. Mc Kay[1], R. Mc Nulty[24], E. Merle[16], C. Meroni[29],
W.T. Meyer[1], A. Miagkov[44], E. Migliore[9], L. Mirabito[27], W.A. Mitaroff[52], U. Mjoernmark[26], T. Moa[46], M. Moch[19],
K. Moenig[9,11], M.R. Monge[15], J. Montenegro[32], D. Moraes[49], P. Morettini[15], G. Morton[36], U. Mueller[54], K. Muenich[54],
M. Mulders[32], L.M. Mundim[6], W.J. Murray[38], G. Myatt[36], T. Myklebust[34], M. Nassiakou[12], F.L. Navarria[5],
K. Nawrocki[53], P. Negri[30], S. Nemecek[13], N. Neufeld[52], R. Nicolaidou[41], P. Niezurawski[53], M. Nikolenko[10,18],
V. Nomokonov[17], A. Nygren[26], A. Oblakowska-Mucha[20], V. Obraztsov[44], A.G. Olshevski[18], A. Onofre[23], R. Orava[17],
K. Osterberg[9], A. Ouraou[41], A. Oyanguren[51], M. Paganoni[30], S. Paiano[5], R. Pain[25], R. Paiva[23], J. Palacios[36],
H. Palka[20], Th.D. Papadopoulou[33], L. Pape[9], C. Parkes[24], F. Parodi[15], U. Parzefall[24], A. Passeri[40], O. Passon[54],
L. Peralta[23], V. Perepelitsa[51], M. Pernicka[52], A. Perrotta[5], C. Petridou[48], A. Petrolini[15], H.T. Phillips[38], F. Pierre[41],
M. Pimenta[23], E. Piotto[9], T. Podobnik[45], V. Poireau[41], M.E. Pol[6], G. Polok[20], P. Poropat[48], V. Pozdniakov[18],
P. Privitera[39], N. Pukhaeva[18], A. Pullia[30], D. Radojicic[36], S. Ragazzi[30], H. Rahmani[33], P.N. Ratoff[22], A.L. Read[34],
P. Rebecchi[9], N.G. Redaelli[30], M. Regler[52], J. Rehn[19], D. Reid[32], R. Reinhardt[54], P.B. Renton[36], L.K. Resvanis[3],
F. Richard[21], J. Ridky[13], G. Rinaudo[47], I. Ripp-Baudot[10], A. Romero[47], P. Ronchese[37], E.I. Rosenberg[1], P. Rosinsky[7],

P. Roudeau[21], T. Rovelli[5], V. Ruhlmann-Kleider[41], A. Ruiz[42], H. Saarikko[17], Y. Sacquin[41], A. Sadovsky[18], G. Sajot[16], L. Salmi[17], J. Salt[51], D. Sampsonidis[12], M. Sannino[15], A. Savoy-Navarro[25], C. Schwanda[52], Ph. Schwemling[25], B. Schwering[54], U. Schwickerath[19], F. Scuri[48], P. Seager[22], Y. Sedykh[18], A.M. Segar[36], R. Sekulin[38], G. Sette[15], R.C. Shellard[6], M. Siebel[54], L. Simard[41], F. Simonetto[37], A.N. Sisakian[18], G. Smadja[27], N. Smirnov[44], O. Smirnova[26], G.R. Smith[38], A. Sokolov[44], O. Solovianov[44], A. Sopczak[19], R. Sosnowski[53], T. Spassov[9], E. Spiriti[40], S. Squarcia[15], C. Stanescu[40], M. Stanitzki[19], A. Stocchi[21], J. Strauss[52], R. Strub[10], B. Stugu[4], M. Szczekowski[53], M. Szeptycka[53], T. Szumlak[20], T. Tabarelli[30], A. Taffard[24], F. Tegenfeldt[50], F. Terranova[30], J. Timmermans[32], N. Tinti[5], L.G. Tkatchev[18], M. Tobin[24], S. Todorova[9], B. Tome[23], L. Tortora[40], P. Tortosa[51], D. Treille[9], G. Tristram[8], M. Trochimczuk[53], C. Troncon[29], M-L. Turluer[41], I.A. Tyapkin[18], P. Tyapkin[26], S. Tzamarias[12], O. Ullaland[9], V. Uvarov[44], G. Valenti[9,5], E. Vallazza[48], C. Vander Velde[2], P. Van Dam[32], W. Van den Boeck[2], W.K. Van Doninck[2], J. Van Eldik[9,32], A. Van Lysebetten[2], N. van Remortel[2], I. Van Vulpen[32], G. Vegni[29], L. Ventura[37], W. Venus[38], F. Verbeure[2], P. Verdier[27], M. Verlato[37], L.S. Vertogradov[18], V. Verzi[29], D. Vilanova[41], L. Vitale[48], E. Vlasov[44], A.S. Vodopyanov[18], G. Voulgaris[3], V. Vrba[13], H. Wahlen[54], A.J. Washbrook[24], C. Weiser[9], D. Wicke[9], J.H. Wickens[2], G.R. Wilkinson[36], M. Winter[10], G. Wolf[9], J. Yi[1], O. Yushchenko[44], A. Zalewska[20], P. Zalewski[53], D. Zavrtanik[45], E. Zevgolatakos[12], N.I. Zimin[18,26], A. Zintchenko[18], Ph. Zoller[10], G. Zumerle[37], M. Zupan[12]

[1]   Department of Physics and Astronomy, Iowa State University, Ames IA 50011-3160, USA
[2]   Physics Department, Univ. Instelling Antwerpen, Universiteitsplein 1, 2610 Antwerpen, Belgium
     and IIHE, ULB-VUB, Pleinlaan 2, 1050 Brussels, Belgium
     and Faculté des Sciences, Univ. de l'Etat Mons, Av. Maistriau 19, 7000 Mons, Belgium
[3]   Physics Laboratory, University of Athens, Solonos Str. 104, 10680 Athens, Greece
[4]   Department of Physics, University of Bergen, Allégaten 55, 5007 Bergen, Norway
[5]   Dipartimento di Fisica, Università di Bologna and INFN, Via Irnerio 46, 40126 Bologna, Italy
[6]   Centro Brasileiro de Pesquisas Físicas, rua Xavier Sigaud 150, 22290 Rio de Janeiro, Brazil
     and Depto. de Física, Pont. Univ. Católica, C.P. 38071 22453 Rio de Janeiro, Brazil
     and Inst. de Física, Univ. Estadual do Rio de Janeiro, rua São Francisco Xavier 524, Rio de Janeiro, Brazil
[7]   Comenius University, Faculty of Mathematics and Physics, Mlynska Dolina, 84215 Bratislava, Slovakia
[8]   Collège de France, Lab. de Physique Corpusculaire, IN2P3-CNRS, 75231 Paris Cedex 05, France
[9]   CERN, 1211 Geneva 23, Switzerland
[10]   Institut de Recherches Subatomiques, IN2P3 - CNRS/ULP - BP20, 67037 Strasbourg Cedex, France
[11]   Now at DESY-Zeuthen, Platanenallee 6, 15735 Zeuthen, Germany
[12]   Institute of Nuclear Physics, N.C.S.R. Demokritos, P.O. Box 60228, 15310 Athens, Greece
[13]   FZU, Inst. of Phys. of the C.A.S. High Energy Physics Division, Na Slovance 2, 180 40, Praha 8, Czech Republic
[14]   Now at D.P.N.C., University of Geneva, Quai Ernest-Ansermet 24, 1211 Geneva 4, Switzerland
[15]   Dipartimento di Fisica, Università di Genova and INFN, Via Dodecaneso 33, 16146 Genova, Italy
[16]   Institut des Sciences Nucléaires, IN2P3-CNRS, Université de Grenoble 1, 38026 Grenoble Cedex, France
[17]   Helsinki Institute of Physics, HIP, P.O. Box 9, 00014 Helsinki, Finland
[18]   Joint Institute for Nuclear Research, Dubna, Head Post Office, P.O. Box 79, 101 000 Moscow, Russian Federation
[19]   Institut für Experimentelle Kernphysik, Universität Karlsruhe, Postfach 6980, 76128 Karlsruhe, Germany
[20]   Institute of Nuclear Physics and University of Mining and Metalurgy, Ul. Kawiory 26a, 30055 Krakow, Poland
[21]   Université de Paris-Sud, Lab. de l'Accélérateur Linéaire, IN2P3-CNRS, Bât. 200, 91405 Orsay Cedex, France
[22]   School of Physics and Chemistry, University of Lancaster, Lancaster LA1 4YB, UK
[23]   LIP, IST, FCUL - Av. Elias Garcia, 14-1°, 1000 Lisboa Codex, Portugal
[24]   Department of Physics, University of Liverpool, P.O. Box 147, Liverpool L69 3BX, UK
[25]   LPNHE, IN2P3-CNRS, Univ. Paris VI et VII, Tour 33 (RdC), 4 place Jussieu, 75252 Paris Cedex 05, France
[26]   Department of Physics, University of Lund, Sölvegatan 14, 223 63 Lund, Sweden
[27]   Université Claude Bernard de Lyon, IPNL, IN2P3-CNRS, 69622 Villeurbanne Cedex, France
[28]   Univ. d'Aix - Marseille II - CPP, IN2P3-CNRS, 13288 Marseille Cedex 09, France
[29]   Dipartimento di Fisica, Università di Milano and INFN-MILANO, Via Celoria 16, 20133 Milan, Italy
[30]   Dipartimento di Fisica, Univ. di Milano-Bicocca and INFN-MILANO, Piazza delle Scienze 2, 20126 Milan, Italy
[31]   IPNP of MFF, Charles Univ., Areal MFF, V Holesovickach 2, 180 00, Praha 8, Czech Republic
[32]   NIKHEF, Postbus 41882, 1009 DB Amsterdam, The Netherlands
[33]   National Technical University, Physics Department, Zografou Campus, 15773 Athens, Greece
[34]   Physics Department, University of Oslo, Blindern, 1000 Oslo 3, Norway
[35]   Dpto. Fisica, Univ. Oviedo, Avda. Calvo Sotelo s/n, 33007 Oviedo, Spain
[36]   Department of Physics, University of Oxford, Keble Road, Oxford OX1 3RH, UK
[37]   Dipartimento di Fisica, Università di Padova and INFN, Via Marzolo 8, 35131 Padua, Italy
[38]   Rutherford Appleton Laboratory, Chilton, Didcot OX11 OQX, UK
[39]   Dipartimento di Fisica, Università di Roma II and INFN, Tor Vergata, 00173 Rome, Italy
[40]   Dipartimento di Fisica, Università di Roma III and INFN, Via della Vasca Navale 84, 00146 Rome, Italy
[41]   DAPNIA/Service de Physique des Particules, CEA-Saclay, 91191 Gif-sur-Yvette Cedex, France
[42]   Instituto de Fisica de Cantabria (CSIC-UC), Avda. los Castros s/n, 39006 Santander, Spain

[43] Dipartimento di Fisica, Università degli Studi di Roma La Sapienza, Piazzale Aldo Moro 2, 00185 Rome, Italy
[44] Inst. for High Energy Physics, Serpukov P.O. Box 35, Protvino, (Moscow Region), Russian Federation
[45] J. Stefan Institute, Jamova 39, 1000 Ljubljana, Slovenia and Laboratory for Astroparticle Physics,
Nova Gorica Polytechnic, Kostanjeviska 16a, 5000 Nova Gorica, Slovenia,
and Department of Physics, University of Ljubljana, 1000 Ljubljana, Slovenia
[46] Fysikum, Stockholm University, Box 6730, 113 85 Stockholm, Sweden
[47] Dipartimento di Fisica Sperimentale, Università di Torino and INFN, Via P. Giuria 1, 10125 Turin, Italy
[48] Dipartimento di Fisica, Università di Trieste and INFN, Via A. Valerio 2, 34127 Trieste, Italy
and Istituto di Fisica, Università di Udine, 33100 Udine, Italy
[49] Univ. Federal do Rio de Janeiro, C.P. 68528 Cidade Univ., Ilha do Fundão 21945-970 Rio de Janeiro, Brazil
[50] Department of Radiation Sciences, University of Uppsala, P.O. Box 535, 751 21 Uppsala, Sweden
[51] IFIC, Valencia-CSIC, and D.F.A.M.N., U. de Valencia, Avda. Dr. Moliner 50, 46100 Burjassot (Valencia), Spain
[52] Institut für Hochenergiephysik, Österr. Akad. d. Wissensch., Nikolsdorfergasse 18, 1050 Vienna, Austria
[53] Inst. Nuclear Studies and University of Warsaw, Ul. Hoza 69, 00681 Warsaw, Poland
[54] Fachbereich Physik, University of Wuppertal, Postfach 100 127, 42097 Wuppertal, Germany

Abstract. Using data collected in the DELPHI detector at LEP-1, measurements of the inclusive τ branching ratios for decay modes containing one, three, or five charged particles have been performed, giving the following results:

$$B_1 \equiv B(\tau^- \to (particle)^- \geq 0\pi^0 \geq 0K^0 \nu_\tau(\bar{\nu})) = (85.316 \pm 0.093 \pm 0.049)\%;$$
$$B_3 \equiv B(\tau^- \to 2h^- h^+ \geq 0\pi^0 \geq 0K^0 \nu_\tau) = (14.569 \pm 0.093 \pm 0.048)\%;$$
$$B_5 \equiv B(\tau^- \to 3h^- 2h^+ \geq 0\pi^0 \geq 0K^0 \nu_\tau) = (0.115 \pm 0.013 \pm 0.006)\%,$$

where h is either a charged π or K meson. The first quoted uncertainties are statistical and the second systematic.

1 Introduction

Historically, there has been an inconsistency in the measured τ exclusive branching ratios: the measurements of exclusive branching ratios to decay modes containing one charged particle did not sum up to the inclusive branching ratio for a charged multiplicity of one. A number of analyses have attempted and succeeded in resolving this question [1–4]. However the current world average values from direct measurements of the topological branching ratios in the Particle Data Group listings [5] have uncertainties which are significantly larger than the values obtained through combined fits to all the τ decay data. In the case of the 1-prong branching ratio (Γ_2 in [5]), the difference between the average and the fit value is more than two standard deviations.

This paper presents a dedicated simultaneous measurement of the decay rates of the τ lepton to different final states as a function of the charged particle multiplicity.

The relevant components of the DELPHI detector and the data-set are described in Sect. 2. The definition of the measured branching ratios and the method used to derive them are introduced in Sect. 3. In Sect. 4 the preselection of the sample of $e^+e^- \to \tau^+\tau^-$ events is described. Section 5 contains a description of the reconstruction of charged particles, as well as the reconstruction algorithms for photons and hadrons which interact with the detector material before the tracking subdetectors. The τ decays are classified according to their charged particle multiplic-

ity. This is described in Sect. 5.4. The results and systematic studies are presented in Sects. 6.1 and 6.2 respectively.

2 Experimental apparatus and data sample

The DELPHI detector and its performance are described in detail elsewhere [6,7]. The subdetector units particularly relevant for this analysis are summarised here. These detector components covered the full solid angle considered in the analysis except where specified, and sat in a 1.2 Tesla solenoidal magnetic field parallel to the z-axis[1].

The reconstruction of charged particles in the barrel region of DELPHI used a combination of the measurements in four different cylindrical subdetectors: a silicon Vertex Detector (VD); the Inner Detector (ID), consisting of a jet chamber tracker and a wire chamber used for trigger purposes; the Time Projection Chamber (TPC); the Outer Detector (OD).

The VD had three layers of silicon micro-strip modules, at radii of 6.3, 9.0 and 11.0 cm from the beam axis. The space point precision was about 8 μm in r-ϕ. For data from 1993 onwards, a measurement of r-z was produced in the

---

[1] In the DELPHI reference frame the origin is at the centre of the detector, coincident with the interaction region, the z-axis is parallel to the e^- beam, the x-axis points horizontally towards the centre of the LEP ring and the y-axis is vertically upwards. The co-ordinates r,ϕ,z form a cylindrical coordinate system, while θ is the polar angle with respect to the z-axis

outermost and innermost layers. This had a precision of about 15 μm. The-two track resolution was 100 μm in r-ϕ and 200 μm in r-z.

The ID had an inner radius of 12 cm and an outer radius of 28 cm. The inner jet chamber part lay at radii below 22 cm. It had a two-track resolution in r-ϕ of 1 mm and a precision in r-ϕ of 50 μm. The outer triggering part was a five-layer wire chamber. This was replaced for the 1995 data with a straw detector containing less material.

The TPC, extending from 30 cm to 122 cm in radius, was the main detector for charged particle reconstruction. The main track reconstruction information was provided by 16 concentric circles of pads which supplied up to 16 three-dimensional space points on a track. In addition, ionisation information was extracted from up to 192 wires. This was used for particle identification purposes. Every $60°$ in ϕ there was a boundary region between read-out sectors about $1°$ wide which had no instrumentation. At $\cos\theta = 0$ there was a cathode plane which caused a reduced tracking efficiency in the polar angle range $|\cos\theta| < 0.035$. The TPC had a two-track resolution of about 3 mm in r-ϕ and 1.5 cm in z.

The OD, with 5 layers of drift cells at a radius of 2 m from the beam axis, was important for the momentum determination of energetic particles.

The principal device for electron and photon identification was the High density Projection Chamber (HPC), located outside the OD, which allowed full reconstruction of the longitudinal and transverse shower components. It covered the polar angle region $|\cos\theta| < 0.75$. In the forward region, $0.800 < |\cos\theta| < 0.985$, the calorimetry was performed by a lead-glass array. For very small polar angles, the calorimetry was performed by the luminosity monitors, the SAT in 1992 and 1993, and the STIC in 1994 and 1995. In the region $0.75 < |\cos\theta| < 0.8$, there was no electromagnetic calorimeter.

Outside the magnet solenoid lay the hadron calorimeter and muon chambers, which were used for hadron and muon identification.

The data were collected by the DELPHI detector from the LEP electron-positron collider, in the years 1992 through 1995, at centre-of-mass energies $\sqrt{s}$ of the e$^+$e$^-$ system between 89 and 93 GeV, on or near to the Z resonance. It was required that the VD, ID, TPC and HPC were in good operational condition for the data sample analysed. The integrated luminosity of the data sample was 135 pb^{-1} of which about 100 pb^{-1} was taken at $\sqrt{s}$ of 91.3 GeV, close to the maximum of the Z boson resonance production cross-section.

The selection procedures were studied with samples of simulated events which had been passed through a detailed simulation of the detector response [7] and reconstructed with the same program as the real data. Separate samples were produced corresponding to the detector configurations in different years. The Monte Carlo event generators used included: KORALZ 4.0 [8] for e$^+$e$^- \to \tau^+\tau^-$ events; DYMU3 [9] for e$^+$e$^- \to \mu^+\mu^-$ events; BABAMC [10] and BHWIDE [11] for e$^+$e$^- \to$ e$^+$e$^-$ events; PYTHIA 5.7 [12] for e$^+$e$^- \to$ q$\bar{\text{q}}$ events. Four-fermion final states

were produced using two different generators. BDK [13] was used for reactions with four leptons in the final state. This included two-photon events where one or two e$^+$ or e$^-$ were not observed in the detector. TWOGAM [14] was used to generate e$^+$e$^- \to$ (e$^+$e$^-$)q$\bar{\text{q}}$ events. The KORALZ 4.0 generator incorporated the TAUOLA 2.5 [15] package for modelling the τ decays. A value of 1.2% was used for the branching ratio of the Dalitz decay $\pi^0 \to \gamma$e$^+$e$^-$.

3 Method

From a high purity sample of $Z \to \tau^+\tau^-$ events, τ decays were identified with charged multiplicity one, three or five, corresponding to the topological branching ratios defined as:

$$B_1 \equiv B(\tau^- \to (particle)^- \geq 0\pi^0 \geq 0K^0\nu_\tau(\bar{\nu}));$$
$$B_3 \equiv B(\tau^- \to 2h^-h^+ \geq 0\pi^0 \geq 0K^0\nu_\tau);$$
$$B_5 \equiv B(\tau^- \to 3h^-2h^+ \geq 0\pi^0 \geq 0K^0\nu_\tau),$$

where h is either a charged π or K meson. In this definition, the K^0_S meson was treated as a neutral particle, even when it decayed to $\pi^+\pi^-$ before the tracking detectors. In τ decays only about 5% of K^0_S mesons decay before the VD. The $h^-K^0(neutrals)\nu_\tau$ component was therefore treated as signal for the 1-prong τ decays and background for the 3-prong τ decays. Although a π^0 meson which decayed to the γe$^+$e$^-$ final state produced two charged particles observed in the detector, it was also treated as a neutral particle, following the τ branching ratio definition given by the Particle Data Group [5]. Thus the branching ratios B_1, B_3 and B_5 correspond to the parameters Γ_2, Γ_{55} and Γ_{101} respectively in [5].

No attempt was made to measure τ decays to more than five charged particles and it was assumed that such decays had a negligible branching ratio. A 90% CL upper limit on the inclusive branching ratio for the τ decay to seven charged particles has been set at 2.4×10^{-6} by the CLEO experiment [16].

At LEP it is possible to separate cleanly $\tau^+\tau^-$ events from other final states, permitting the efficient selection of a high purity τ sample. One can measure the branching ratio $B(\tau \to X)$ for the decay of the τ to a final state X using the expression

$$B(\tau \to X) = \frac{N_X}{N_\tau} \cdot \frac{1 - b_X}{1 - b_\tau} \cdot \frac{\epsilon_\tau}{\epsilon_X}, \quad (1)$$

where N_X is the number of identified decays of type X found in the sample of N_τ τ-decay candidates, preselected with efficiency ϵ_τ with a background fraction of b_τ. ϵ_X is the total (preselection $\times$ identification) efficiency for selecting the decay mode $\tau \to X$, with a background fraction of b_X, including background from other τ decay modes. In a $\tau^+\tau^-$ event selection without specific requirements on either of the two τ candidates in the event, ϵ_τ will be identical to the $\tau^+\tau^-$ event selection efficiency.

In the case where several branching ratios are measured simultaneously, candidate τ decays can be classified as a function of the detector components used in the charged particle track reconstruction. These classes (detailed in Sect. 5.4) typically have different signal to background ratios for different types of decays and thus contain different levels of information. To obtain the branching ratios, a fit can then be performed to the predicted number $N_{i,pred}$ of decays in a class i:

$$N_{i,pred} = N_\tau(\epsilon_{i,1}B_1 + \epsilon_{i,3}B_3 + \epsilon_{i,5}B_5) + N_{i,bkg} \ , \quad (2)$$

where $\epsilon_{i,m}$ is the probability of a τ decay of true multiplicity m being attributed to class i and $N_{i,bkg}$ is the estimated background in class i due to non-$\tau^+\tau^-$ events. This can be extended to a simultaneous fit for both τ decays in a candidate $\tau^+\tau^-$ event. The predicted number $N_{i,j,pred}$ of $\tau^+\tau^-$ events with one τ decay in class i and the other in class j is

$$N_{i,j,pred} = N_{\tau\tau} \sum_{m,n} \epsilon_{ij}^{mn} B_m B_n + N_{i,j,bkg} \ , \quad (3)$$

where $N_{i,j,bkg}$ is the estimated number of non-$\tau^+\tau^-$ background events in class i,j and ϵ_{ij}^{mn} is the probability of an event with decays of true multiplicity m and n being attributed to class i,j. $N_{\tau\tau}$ is the number of $\tau^+\tau^-$ events and can be left free and obtained from a fit to the different classes. This method takes into account correlations between the two observed τ decays in an event and has the advantage that non-$\tau^+\tau^-$ backgrounds tend to populate event classes which have correlations between the two candidate τ decays (e.g. dimuons in the 1-versus-1 topology but not in 1-versus-3) and thus exhibits less sensitivity to backgrounds. It was used as the principal method in the following analysis.

4 $e^+e^- \rightarrow \tau^+\tau^-$ preselection

In $e^+e^- \rightarrow Z \rightarrow \tau^+\tau^-$ events at $\sqrt{s} = M_Z$, the τ^+ and τ^- are produced back-to-back, ignoring radiative effects. Each τ decays, producing one, three, or more charged particles in addition to one or two neutrinos and, possibly, neutral mesons. All particles apart from the neutrinos can be detected in DELPHI. A $\tau^+\tau^-$ event is thus characterised by two low multiplicity jets which appear approximately back-to-back in the laboratory. The loss of the neutrinos implies that not all the energy in the event is seen in the detector.

Except where explicitly stated, all quantities calculated using charged particles used only charged particle tracks which had hits in at least the TPC or OD, to ensure good momentum reconstruction from the long track length, and had an impact parameter with respect to the centre of the interaction region of less than 1.5 cm in r-ϕ and 4.5 cm in z. The basic $e^+e^- \rightarrow \tau^+\tau^-$ preselection described below has some differences compared with that used previously in studies of the τ leptonic branching ratios [17]. There are slightly modified cuts to reduce non-τ backgrounds and the addition of subsamples of events

containing τ decays with a nuclear reinteraction in the detector material and τ decays where one charged particle was reconstructed only in the VD and ID tracking subdetectors.

4.1 Preselection criteria

To ensure that the τ decay products were in the region of DELPHI corresponding to the HPC acceptance, the thrust axis of the event, calculated using only charged particle tracks, was required to lie in the polar angle region defined by $|\cos\theta| < 0.732$. The event was split into two hemispheres, each associated to a candidate τ decay, by the plane perpendicular to the thrust axis and containing the point at the centre of the interaction region. Each hemisphere had to contain at least one charged particle. It was required that at least one charged particle lie in the polar angle region defined by $|\cos\theta| > 0.035$ in order to reduce the effects of the TPC tracking inefficiency near $\cos\theta = 0$.

Most hadronic Z decays were rejected by requiring that the event contain at most eight charged particle tracks with hits in either the TPC or OD and satisfying the impact parameter cuts described above.

Four-fermion events were suppressed by requiring that the event isolation angle be greater than 160°. This was defined as the minimum angle between any pair of charged particles in opposite τ decay hemispheres.

Backgrounds from $\mu^+\mu^-$ and e^+e^- final states and cosmic rays were reduced by requiring that the isolation angle be less than 179.5° for events with only two charged particles.

The $\mu^+\mu^-$ and e^+e^- contamination was reduced further by requiring that both $p_{rad} = \left(\frac{|\mathbf{p}_1|^2}{p_1'^2} + \frac{|\mathbf{p}_2|^2}{p_2'^2}\right)^{1/2}$ and $E_{rad} = \left(\frac{E_1^2}{E_1'^2} + \frac{E_2^2}{E_2'^2}\right)^{1/2}$ be less than unity. The variables $\mathbf{p}_1$ and $\mathbf{p}_2$ are the momenta of the highest momentum charged particles in hemispheres 1 and 2 respectively. The quantity p_1' was obtained from the formula

$$p_1' = \sqrt{s}\sin\theta_2/(\sin\theta_1 + \sin\theta_2 + |\sin(\theta_1 + \theta_2)|) \ , \quad (4)$$

and p_2' by analogy with the indices 1 and 2 interchanged. The angles θ_1 and θ_2 are the polar angles of the highest momentum charged particle in hemispheres 1 and 2 respectively. The variables E_1 and E_2 are the total electromagnetic energies deposited in cones of half-angle 30° about the momentum vectors $\mathbf{p}_1$ and $\mathbf{p}_2$ respectively, while $E_j' = cp_j'$, for $j = 1, 2$. These definitions of p_{rad} and E_{rad} are identical to those used for the $e^+e^- \rightarrow \tau^+\tau^-$ measurements at LEP-2 [18]. They take into account more correctly the radiative events where the radiative photon is close to the beam axis than the definition used previously in LEP-1 analyses [17,19]. In the limit of no radiation the new and old definitions are equivalent. The distributions of p_{rad} and E_{rad} are shown in Fig. 1a and Fig. 1b respectively, after all cuts have been imposed except the one on the displayed variable. There are some
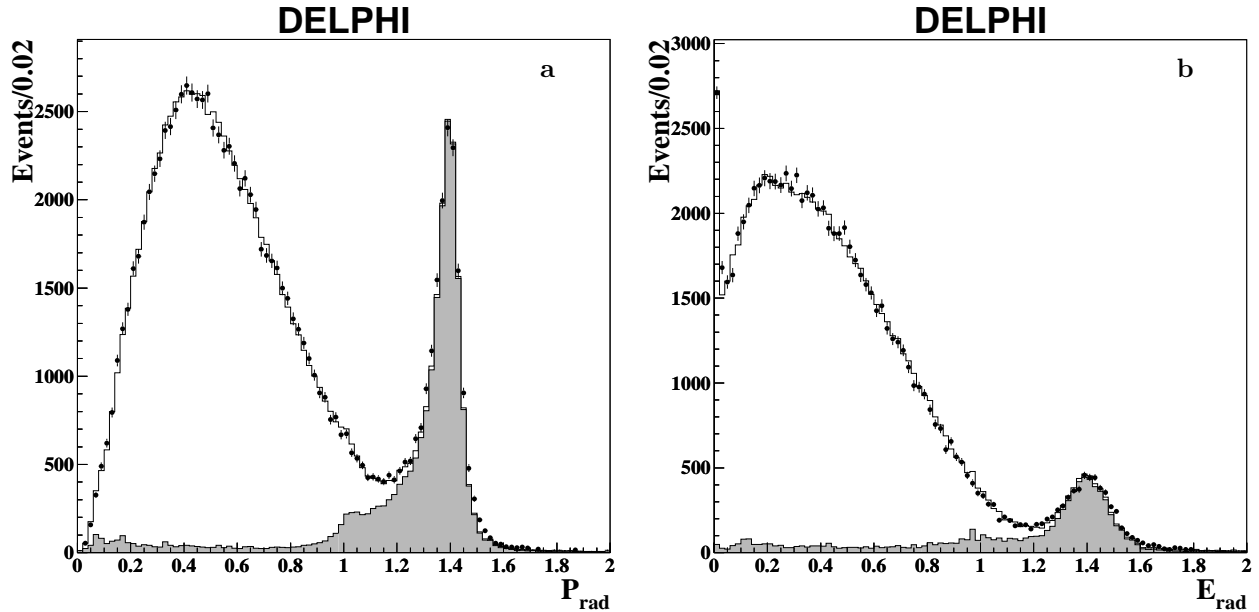
Fig. 1a,b. Distributions of **a** p_{rad} and **b** E_{rad} variables used in $\tau^+\tau^-$ selection. The dots are data, the line is simulation. The shaded area is non-$\tau^+\tau^-$ background. In both cases the selected sample lies in the region below a cut at 1.0. The spike in the first bin of plot **b** is due to events where both τ's decay to either a muon or a charged hadron which does not interact in the HPC. This bin has been scaled down by a factor two for presentational purposes

small data/simulation discrepancies in the momentum resolution, visible in the dimuon peak at $p_{rad} \approx 1.4$. This had a negligible effect on the analysis.

Much of the remaining background from the dileptonic channels came from events containing hard radiation lying far from the beam. These events should lie in a plane. Where two charged particles and a photon were visible in the detector, such events were removed by requiring that the sum of the angles between the three particles was greater than 359.8°.

A further reduction in four-fermion background was achieved by requiring a minimum visible energy in the event. The visible energy E_{vis} is the sum of the energies of all charged particles and the electromagnetic energies of all neutral particles, neglecting energy deposits recorded by the very forward calorimeters (SAT and STIC) at angles of less than 12° from the beam axis. Events were accepted if E_{vis} was greater than $0.09 \times \sqrt{s}$. For events with only two charged particles, an additional condition was applied that the vectorial sum of the charged particle momenta in the r-ϕ plane be greater than 0.4 GeV/c. Four-fermion events typically have very low values of of this quantity compared with $\tau^+\tau^-$ events.

Most cosmic rays were rejected by the upper cut on isolation angle. Further rejection was carried out by requiring at least one charged particle in the event have an impact parameter with respect to the interaction region of less than 0.3 cm in the r-ϕ plane and that in the τ decay hemisphere opposite to this particle at least one charged particle have an impact parameter in the r-ϕ plane of less than 1.5 cm. It was also required that both event hemispheres have a charged particle track whose perigee point lay within 4.5 cm of the interaction region in z.

Additional $\tau^+\tau^-$ events were selected where one of the τ's produced a 1-prong decay and the other τ decay produced one charged hadron which interacted with the detector material inside the TPC and where the interaction was reconstructed by the nuclear reinteraction reconstruction algorithm described in Sect. 5.3. The cuts in p_{rad} and E_{rad} were not applied. This increased the selection efficiency by about 1% with a relative background of 0.8%.

A further class of events was selected where one of the τ decays left one charged particle track with hits in only the VD and the ID due to inefficiencies in the TPC and OD. Many of these tracks contained no polar angle information and had poor momentum resolution, so they were excluded from the calculation of event quantities such as the thrust or p_{rad}. The p_{rad} requirement was replaced with a cut on the momentum of the highest momentum charged particle in the opposite hemisphere, requiring it to be less than 90% of the beam momentum. This cut was tightened to 70% if there was an identified muon in the hemisphere. This subsample of events contributed an extra 4% of events with a relative background of 5%.

The total efficiency, including all classes of events, was estimated from simulation to be $(51.74 \pm 0.04)\%$. This corresponds to an efficiency of approximately 85% within the angular acceptance cuts.

4.2 Backgrounds

Knowledge of the background from q$\bar{q}$ events is of particular importance in this analysis as it constitutes a serious background in the higher multiplicity topologies. Uncertainties in the low multiplicity backgrounds have a reduced
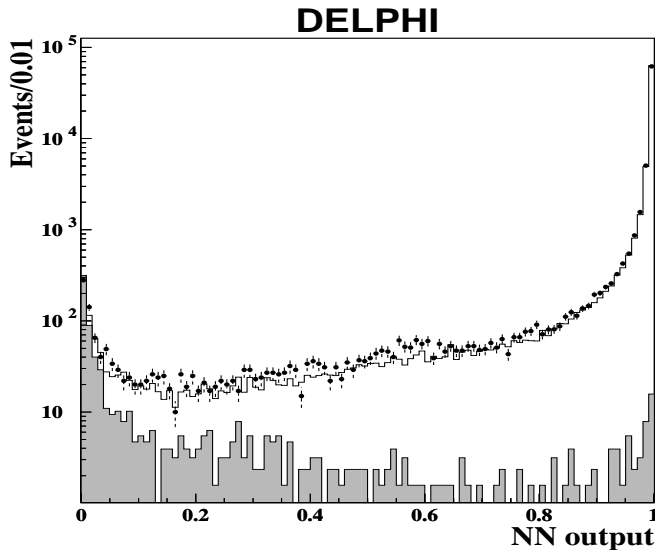
Fig. 2. The output neuron distribution for the neural network used for the final $q\bar{q}$ rejection. The dots are data, the line is simulation and the shaded region shows the simulated $q\bar{q}$ contribution. The selected events lie in the region with output neuron values above 0.05

effect on the measured branching ratios due to the large B_1 value and the resultant cancellation in (1). After the cuts described above, the $q\bar{q}$ background estimated from simulation is $(0.80 \pm 0.05)\%$, where the error is purely statistical. To reduce systematic effects due to $q\bar{q}$ background, a further level of rejection was performed. A number of observables display separation power between $\tau^+\tau^-$ and $q\bar{q}$ events while being only weakly dependent on the topology classification. These were: the isolation angle; the event thrust; the number of neutral electromagnetic showers in an event; the invariant masses reconstructed using charged particles in each candidate τ decay hemisphere of an event, and the invariant masses reconstructed using both charged and neutral particles in each candidate τ decay hemisphere. These variables were used as inputs to a neural network with one hidden layer of eight neurons and a single output neuron. The output neuron distribution is shown in Fig. 2. A cut at 0.05 in the output neuron gave a rejection factor of about three, leaving a background of 0.29% from $e^+e^- \rightarrow q\bar{q}$, while rejecting only 1.3×10^{-3} of the remaining $\tau^+\tau^-$ events. Discrepancies between data and simulation in this variable are discussed in Sect. 6.2.1.

Background levels were estimated as accurately as possible using the data. Variables sensitive to a particular type of background were chosen. The background levels were extracted by fitting for the background contribution in these variables assuming the background shape from the simulation. Typically a relative precision of order 10% or better was achieved, ensuring systematic uncertainties on the topological branching ratios below the expected statistical precision.

The background from $e^+e^- \rightarrow q\bar{q}$ was estimated using the data by performing a fit to the distribution of the neural network output neuron. The shape of the background

distribution was taken from simulation and the fit was performed for the normalisation factor. A factor 0.92 ± 0.03 was obtained compared to the simulation.

The background due to the fully leptonic four-fermion final states was estimated from the data by extrapolating from the observed background in the low isolation angle region for events with a low visible energy, as well as for events tagged by the presence of a muon (for $e^+e^-\mu^+\mu^-$) or an electron (for $e^+e^-e^+e^-$). The relative uncertainty obtained on the normalisation for these final states was $\pm 10\%$. Figure 3 shows the isolation angle distributions for different classes of events.

The background from dimuon events in the $\tau^+\tau^-$ sample was estimated by studying the momentum distribution for high momentum identified muons, and by studying the p_{rad} distributions for events with two identified muons. This yielded a correction factor relative to the simulation of 0.96 ± 0.03. The p_{rad} distribution, after all other $\tau^+\tau^-$ preselection cuts, of events containing two identified muons is shown in Fig. 4a. Similar studies were carried out for Bhabha background using the associated electromagnetic energy and anti-electron tagging in the hadron calorimeter and muon chambers. This, combined with studies [17] comparing the BHWIDE and BABAMC Bhabha generators indicated that a rescaling upwards by 1.15 ± 0.15 of the Bhabha background estimated from simulation was necessary. In addition, further cross-checks were performed by studying the p_{rad} and E_{rad} distributions in the region outside the one occupied by $\tau^+\tau^-$ events. The E_{rad} distribution, after all other $\tau^+\tau^-$ preselection cuts, for events with two identified electrons is shown in Fig. 4b.

The cosmic ray contamination was estimated from the data to be $(50\pm8) \times 10^{-5}$ by extrapolating from the number of events seen outside the cuts in impact parameter.

The total background was estimated to be $(1.51 \pm 0.10)\%$, with the following breakdown: $(0.11\pm0.01)\%$ from $\mu^+\mu^-$ final states; $(0.40 \pm 0.07)\%$ from Bhabha events; $(0.29 \pm 0.01)\%$ from $q\bar{q}$ events; $(0.27 \pm 0.03)\%$ from $e^+e^- e^+e^-$ final states; $(0.10 \pm 0.01)\%$ from $e^+e^-\mu^+\mu^-$ events; $(0.27\pm0.03)\%$ from $e^+e^-\tau^+\tau^-$ final states; $(0.02\pm0.01)\%$ from $e^+e^-q\bar{q}$ final states; $(0.05\pm0.01)\%$ from cosmic rays. The background from $\mu^+\mu^-\mu^+\mu^-$, $\mu^+\mu^-\tau^+\tau^-$ and $\tau^+\tau^-\tau^+\tau^-$ final states was negligible.

Satisfactory agreement with the simulation was observed for each year separately, and estimated efficiencies and backgrounds were compatible between the different years.

5 Topology reconstruction

5.1 Charged particle tracking

The charged particle track pattern recognition was based on a robust algorithm designed to minimise the number of bad associations between hits produced by different particles in the different elements of the tracking system. In general, most tracks contain hits in all the tracking subdetectors, the VD, ID, TPC and OD. Most importantly,

DELPHI
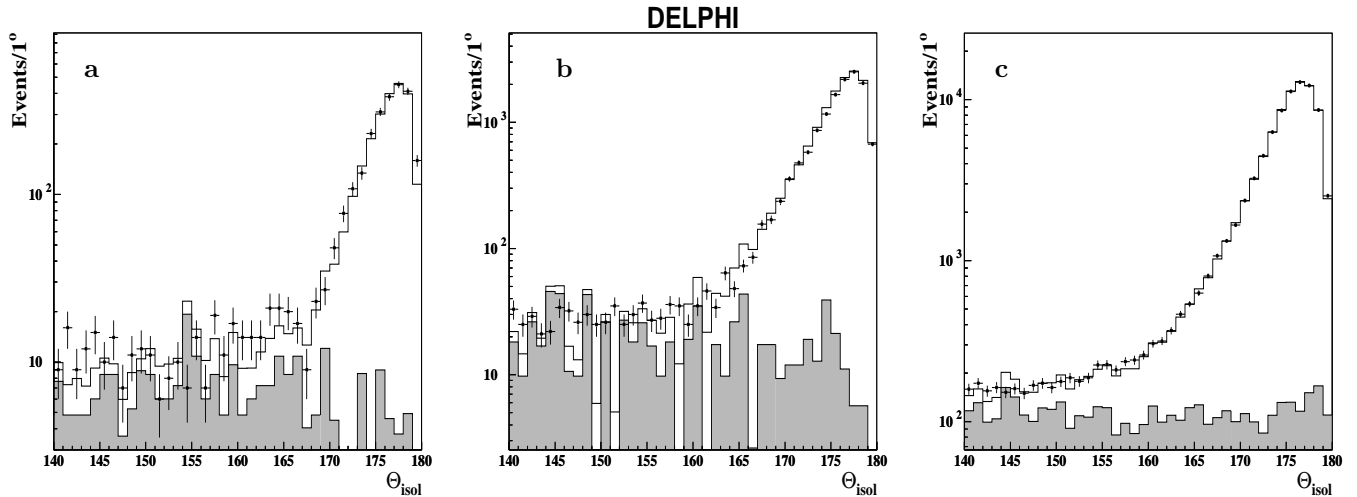
Fig. 3a–c. Distributions of isolation angle (in degrees) in candidate $\tau^+\tau^-$ events: **a** events containing two identified muons; **b** events containing at least one tagged electron; **c** all events in the $\tau^+\tau^-$ sample. In all cases data are the dots and simulation is the line. In **a** and **b** the shaded area is the four-fermion background, while in **c** it contains all background contributions

DELPHI   **DELPHI**
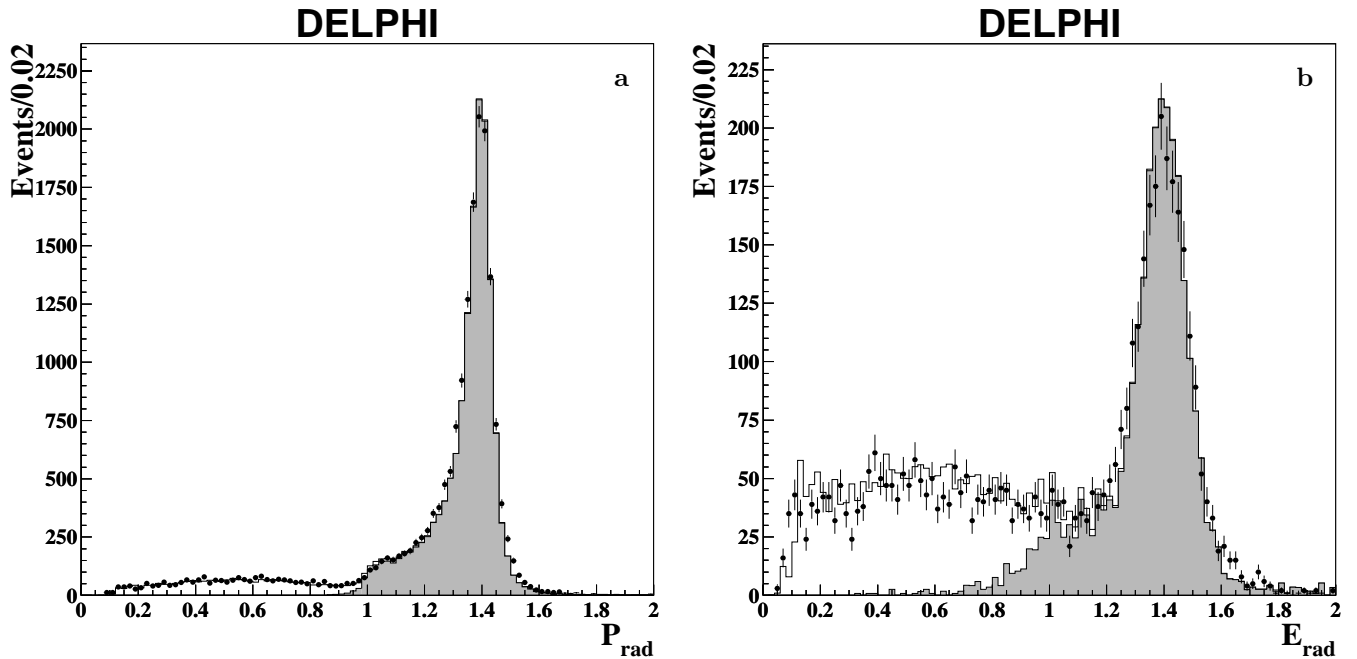
Fig. 4a,b. Distributions used in the study of the dileptonic background to the $\tau^+\tau^-$ preselection: **a** p_{rad} distribution for events containing two identified muons; **b** E_{rad} distribution for events containing two identified electrons. In both cases the dots are the data and the line is simulation. In **a** the shaded area is the background contribution due to the reaction $e^+e^- \to \mu^+\mu^-(\gamma)$, while in **b** it is the background contribution from $e^+e^- \to e^+e^-(\gamma)$ events

for the rejection of photon conversion products, the attachment of VD hits to a track must be as efficient and as unambiguous as possible. The VD efficiency and misassociation probability in simulation have been tuned to the data with $e^+e^- \to \mu^+\mu^-$ events and with large samples of hadronic events for the purposes of heavy quark tagging [20].

The TPC was the most important subdetector for charged particle reconstruction. The section of a track reconstructed in the TPC had to contain at least three space points out of a maximum possible 16. In dense topologies, where tracks lay closer together than the inherent two-track resolution of the detector, the clustering algorithm used to reconstruct space points used the information contained in the ϕ profile of a single cluster to resolve two tracks down to distances of typically 2 to 3 mm in r-ϕ. Where tracks were closer than this, a space point was associated simultaneously to each of the tracks with which it was compatible and assigned a large error so as not to introduce systematic biases in the reconstructed parame-

ters for these tracks. For regions away from the TPC sector boundaries, the probability to include either the TPC or the OD on an isolated track was close to 100%.

After the data had been passed through the standard algorithm, a second algorithm was run which produced VD-ID tracks from combinations of hits in the VD and the ID jet chamber. This algorithm recuperated charged particle tracks around the boundary regions of the TPC or cases where the two-track resolution of the TPC prevented it from resolving both charged particles. The two-track resolution of the VD is more than one order of magnitude better in r-ϕ than the TPC. However the VD-ID tracks had poorly reconstructed momenta and particle charge sign determination due to their short length. This had no consequences for the charged particle multiplicity reconstruction.

5.2 Photon conversions

A good understanding of the photons converting in material before the tracking subdetectors is important in order to measure correctly the true charged particle multiplicity in a τ decay. About 7% of photons interact with the material before the TPC gas volume, giving an e$^+$e$^-$ pair detected in some of the tracking chambers. In particular, unreconstructed conversions form an important potential background from lower multiplicity topologies in higher multiplicity samples. Furthermore, to measure in data both the conversion reconstruction efficiency and the amount of material, it was necessary to study the rate of both reconstructed and unreconstructed converted photons.

Converted photons were reconstructed using the algorithms described below. These are described in more detail in [21]. Photons converting in the beam-pipe, VD, ID and TPC inner wall were reconstructed using charged particle tracks observed in the TPC. For each TPC track the position of the tangent to the helix which passed through the interaction region was calculated. This point gave the estimated position of the conversion. All tracks for which this point was compatible with the interaction region within one standard deviation were neglected as conversion candidates. If two conversion candidates were found with compatible conversion points, they were accepted as a converted photon provided that: the two tracks had opposite curvature; the mean conversion radius of the two tracks was greater than 5 cm; at least one of the tracks had no associated point inside the mean conversion radius; the angles of the two tracks at the conversion radii agreed within 30 mrad in ϕ and 15 mrad in θ. This algorithm had an efficiency, estimated from simulation, of about 60% for photon energies below 6 GeV falling to about 20% at 10 GeV. It was complemented by an algorithm using a fit to a joint origin for two charged particle tracks assuming zero opening angle, with similar requirements on the position of the reconstructed conversion radius to the previous algorithm. This had an efficiency of about 40% for photon energies above 8 GeV. The average efficiency for the combination of both algorithms was $(68.1 \pm 0.2)\%$ for

the photon energy spectrum in simulated 1-prong τ decays and $(59.8 \pm 0.4)\%$ for 3-prong decays.

In 3-prong decays, the probability of reconstructing a $\pi^+\pi^-$ pair incorrectly as a photon conversion was estimated from simulation to be 1×10^{-4}. For systematic studies the uncertainty on this was taken as 100% of the size of the effect. The probability of reconstructing a $K_S^0 \to \pi^+\pi^-$ decay incorrectly as a photon conversion was estimated from simulation to be 1.5%, however this did not alter the observed charged particle multiplicity.

The rates of reconstructed and unreconstructed converted photons were studied as a function of the radial coordinate of the estimated conversion point. The conversions were separated into those taking place in the beam-pipe, VD and ID jet chamber inner wall, the ID jet chamber sensitive volume, the ID jet chamber outer wall and ID Trigger Layers, and the TPC inner wall. The bulk of the material was in the TPC inner wall. In order to be as independent as possible of the $\tau^+\tau^-$ presample and modelling of the photon production rate in τ decays, the study was performed using e$^+$e$^- \to \mu^+\mu^-\gamma$ and e$^+$e$^- \to$ e$^+$e$^-\gamma$ radiative events. The events were selected using electron or muon identification and used kinematic constraints to predict the direction and energy of the photon. The rates were recorded for events with an HPC shower, reconstructed conversion, or no reconstructed conversion but some charged particle tracks consistent with an electron-positron pair arising from a converted photon. In the latter case the radius of the conversion point was taken as being that of the material layer lying just inside the innermost first measured point on either of the two tracks believed to be due to the conversion. The rates were normalised to the total number of observed photons, including conversions. The identical procedure was applied to the simulation. Correction factors for the reconstructed conversion rate were obtained from the ratio A_{rec}^{conv} of the rates R_d^{rec} and R_s^{rec} of reconstructed conversions in data and simulation respectively. Analogous correction factors for the unreconstructed conversion rate were obtained from the ratio A_{unrec}^{conv} of the rates R_d^{unrec} and R_s^{unrec} of unreconstructed conversions.

The measured correction factors were used to estimate the reconstruction efficiency and amount of material. The ratio A_{rec}^{conv} is given by

$$A_{rec}^{conv} = \frac{R_d^{rec}}{R_s^{rec}} = \frac{R_d^0}{R_s^0} \cdot \frac{X_d^{EM}}{X_s^{EM}} \cdot \frac{\epsilon_d^{conv}}{\epsilon_s^{conv}}. \qquad (5)$$

The subscripts d and s stand for data and simulation respectively. $R_{d,s}^0$ is the total rate of photons, $X_{d,s}^{EM}$ is the probability of a conversion taking place (proportional to the amount of material in terms of radiation lengths) and $\epsilon_{d,s}^{conv}$ is the reconstruction efficiency. The ratio A_{unrec}^{conv} is given by

$$A_{unrec}^{conv} = \frac{R_d^{unrec}}{R_s^{unrec}} = \frac{R_d^0}{R_s^0} \cdot \frac{X_d^{EM}}{X_s^{EM}} \cdot \frac{1 - \epsilon_d^{conv}}{1 - \epsilon_s^{conv}}. \qquad (6)$$
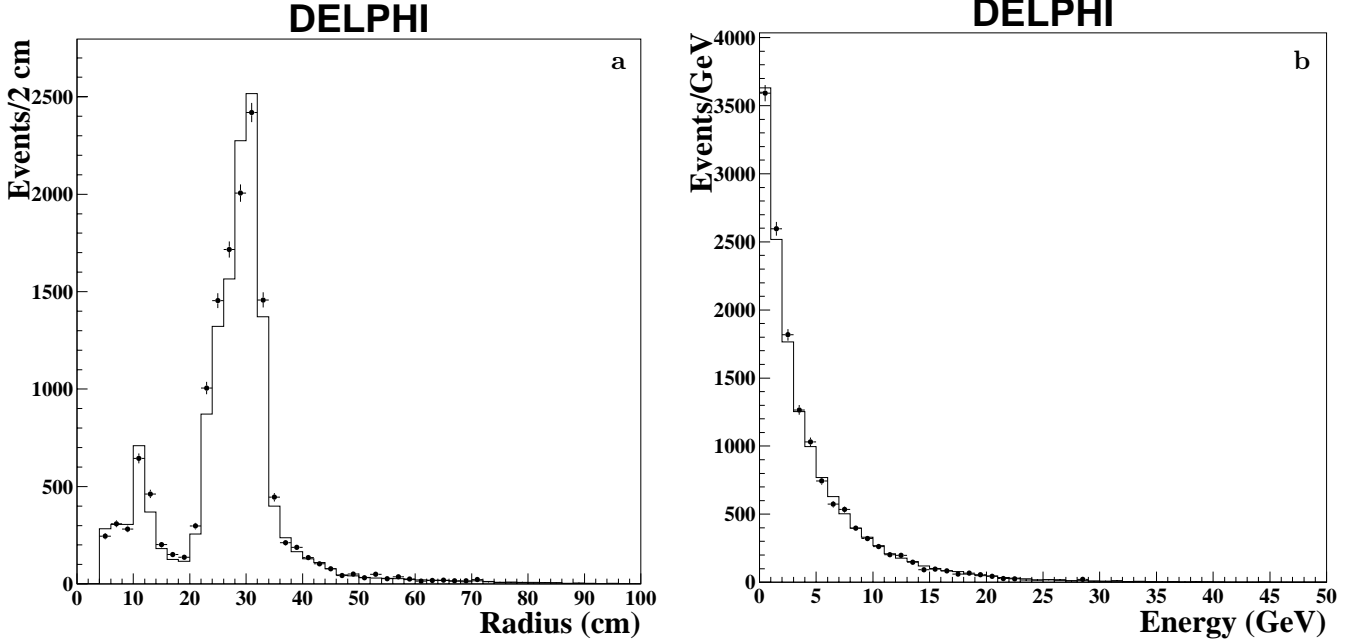
Fig. 5. a Distribution in $e^+e^- \to \tau^+\tau^-$ events of the estimated conversion radius for photons converted in front of the TPC. Data are dots, the line is simulation after applying correction factors from $e^+e^- \to \mu^+\mu^-\gamma$ and $e^+e^- \to e^+e^-\gamma$ events. **b** Reconstructed conversion photon energy in $e^+e^- \to \tau^+\tau^-$ events. Data are dots, the line is simulation after applying correction factors

The conversion reconstruction efficiency in data ϵ_d^{conv} can be obtained from the data alone via the relation

$$\epsilon_d^{conv} = \frac{R_d^{rec}}{R_d^{rec} + R_d^{unrec}}, \qquad (7)$$

independently of any assumptions on the material or, if R_d^{rec} and R_d^{unrec} are measured on the same data sample, on the incident photon flux. If the ratio R_d^0/R_s^0 is known, measurements of A_{rec}^{conv}, A_{unrec}^{conv} and ϵ_d^{conv}, combined with ϵ_s^{conv} from the simulation, can provide an estimation of the material ratio X_d^{EM}/X_s^{EM} for electromagnetic interactions. The ratio R_d^0/R_s^0 of the rates of photons produced in the $e^+e^- \to \mu^+\mu^-\gamma$ and $e^+e^- \to e^+e^-\gamma$ radiative events was taken to be unity with a systematic uncertainty of $\pm 2\%$ [22].

The factors A_{rec}^{conv} and A_{unrec}^{conv} obtained as a function of interaction radius are given in Table 1. These factors were used to reweight the simulated events used in the estimation of the selection efficiencies to account for data/simulation discrepancies in the material and reconstruction efficiency. The distributions of the conversion radius and energy for reconstructed converted photons are shown in Fig. 5, where the simulation has been corrected with the factors obtained in the $e^+e^- \to \mu^+\mu^-\gamma$ and $e^+e^- \to e^+e^-\gamma$ events. There are still some localised discrepancies between data and simulation due to simplifications in the detector material description in the simulation program. For the τ presample, the rate of reconstructed conversions observed in data was 1.004±0.008 times that predicted by the simulation after the application of the correction factors, in excellent agreement.

The data taken in different years were studied separately, in particular before and after the beginning of 1995, the point after which the material in the ID trigger layers was substantially reduced. Consistency was observed between the different years and the change in conversion rate observed in the ID trigger layers between 1992-1994 and 1995 was consistent with the expectation.

The conclusion, integrating up to a radius of 50 cm, is that the material is underestimated in the detector simulation by about 10% in terms of radiation lengths, while the conversion reconstruction algorithm efficiency is similar in data and simulation.

The kinematical conversion reconstruction was complemented by conversion rejection based on an electron identification algorithm [7] which combined information from the TPC ionisation and the HPC electromagnetic shower reconstruction. This algorithm also rejected many π^0 Dalitz decays, which was particularly important for rejecting backgrounds in the 5-prong τ decay sample. A conversion was flagged if there was at least one tightly tagged electron in a hemisphere with greater than one track in the TPC or if there were a pair of oppositely charged particles both of which were loosely tagged as electrons. These criteria were chosen to minimise the probability of misidentifying a $\pi^+\pi^-$ pair as e^+e^- rather than to maximise the conversion identification efficiency. In simulation, the efficiency to reject the remaining conversions was (59.6±0.6)% in 1-prong decays and (54.5±0.8)% in 3-prong decays. The electron-positron pair rejection also identified (72.7±1.2)% of Dalitz pairs from π^0 decays in simulated 1-prong decays, giving an improved classification for these decays. The efficiency was (68.3±3.1)% for 3-prong decays. The efficiency to identify Dalitz pairs was

Table 1. Factors used to correct simulated photon conversions and data/simulation discrepancies as a function of the radius of the interaction point. Column 5 shows the data/simulation ratio of reconstruction efficiency and column 6 the equivalent ratio for the material

Radius		Conversions			
Lower	Upper	A_{rec}^{conv}	A_{unrec}^{conv}	$\epsilon_d^{conv}/\epsilon_s^{conv}$	X_d^{EM}/X_s^{EM}
0cm	13.0cm	1.00 ± 0.03	1.14 ± 0.05	0.96 ± 0.03	1.04 ± 0.03
13.0cm	22.0cm	1.34 ± 0.05	1.70 ± 0.12	0.93 ± 0.06	1.45 ± 0.05
22.0cm	28.5cm	1.23 ± 0.03	1.50 ± 0.09	0.94 ± 0.05	1.31 ± 0.03
28.5cm	50cm	1.04 ± 0.02	0.91 ± 0.04	1.04 ± 0.03	1.00 ± 0.02
0cm	50cm	1.10 ± 0.01	1.09 ± 0.03	1.00 ± 0.02	1.09 ± 0.02
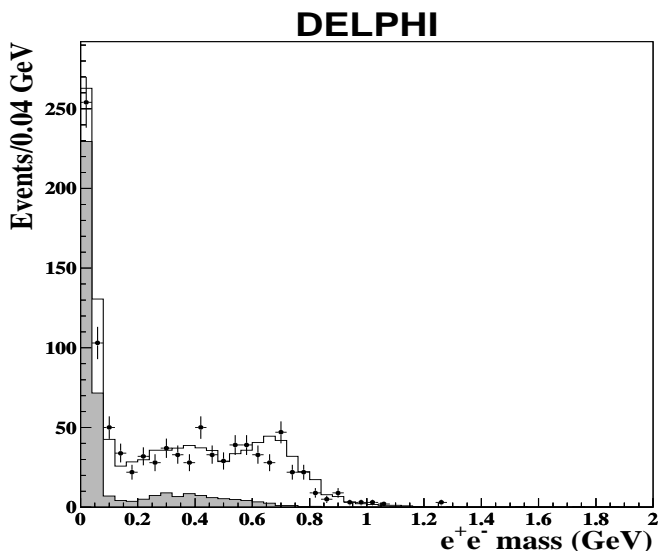
Fig. 6. Invariant mass $m_{e^+e^-}$ distributions for pairs of oppositely charged particles with one or both particles identified as electron candidates and where both tracks have hits in the VD. Data are dots, the simulation is the line. The shaded area shows the contribution from $\pi^0 \to \gamma e^+e^-$ decays. The region $m_{e^+e^-} > 200$ MeV is dominated by misidentified $\pi^+\pi^-$ pairs

higher than for conversions due to biases arising from the kinematic conversion reconstruction algorithm which had already identified and reconstructed most converted photons.

The conversion rejection efficiency of the electron identification algorithm was cross-checked in τ decays containing three charged particle tracks, from the rate of oppositely charged pairs of particles which satisfied the electron tagging requirements outlined above and where neither particle had a hit in the VD. The ratio of the efficiency in data to that in simulation was estimated to be 0.96 ± 0.05, in good agreement with unity. The relative systematic uncertainty on the efficiency of this algorithm was conservatively taken to be 10%, to account for any systematic effects in the estimation of the ratio and in its application to all classes of charged particle tracks.

Figure 6 shows the invariant mass distribution for pairs of oppositely charged particles in τ decay hemispheres containing three charged particles, where one or both of the

pair were tagged as an electron candidate and where both tracks had hits in the VD. The electron mass was assumed for both particles. The VD association requirement rejected most photon conversions, which occurred after the VD, while not affecting the signal of π^0 Dalitz decays, or of hadrons misidentified as electrons. The contribution from Dalitz decays peaks at low masses, below the π^0 mass. The tail from Dalitz decays in the region of masses around 200 MeV to 600 MeV arises from decays where only one of the electron or positron was identified and there were two possible combinations of oppositely charged particles. In such decays only half the possible combinations were due to the e^+e^- pair. In these cases each combination has been given a weight of one half. The region of mass greater than 200 MeV was dominated by $\pi^+\pi^-$ pairs where one of the pions was misidentified as an electron. This permitted a determination from the data of the probability to misidentify a 3-prong τ decay as a 1-prong decay containing a conversion candidate. The misidentification probability was estimated to be (1.29 ± 0.09)%. The uncertainty was dominated by data statistics and contained a contribution from the VD association efficiency. From the ratio of data to simulation in the low mass spike it was estimated that the efficiency to reject a π^0 Dalitz decay in data was 0.90 ± 0.07 times the efficiency obtained in simulation. The uncertainty included contributions from the error on the Particle Data Group best estimation of the $\pi^0 \to \gamma e^+e^-$ branching ratio [5], the uncertainty in the VD efficiency and the limited simulation statistics in addition to the statistical uncertainty. No correction was applied to the simulation and a relative uncertainty of 10% on the Dalitz rejection efficiency was taken.

Most δ-rays were rejected by the requirement of VD hits on a track. Events in simulation containing a δ-ray were reweighted with the radius dependent factors describing the ratio of material in terms of radiation lengths X_d^{EM}/X_s^{EM} in Table 1. There is some ambiguity in the choice of this factor. The associated systematic uncertainties are discussed in Sect. 6.2.3.

5.3 Nuclear reinteractions

About 3% of hadrons reinteract inelastically with the material before the TPC gas volume, and produce typically up to 10 charged secondary particles. These reinteractions

were reconstructed by an algorithm which was designed to find secondary reinteraction vertices using the tracks from outgoing charged particles produced in nuclear reinteractions.

The algorithm was robust with respect to the number of charged particles produced and to the position of the reinteraction with the DELPHI detector material. Only tracks which had impact parameters inconsistent with coming from the interaction region were considered. The algorithm iterated over all pairs of tracks, and attempted to fit a vertex in three dimensions if neither of the tracks had already been included in an earlier successfully fitted vertex. However, if one of the tracks had already been included in an earlier fitted vertex, an attempt was made to include the other track in that vertex. This was the main part of the algorithm permitting the reconstruction of vertices with an arbitrary number of outgoing charged particle tracks. In the rare case where both tracks had already been associated to different fitted vertices, an attempt was made to merge those two vertices, if their positions were compatible. In all cases a candidate reinteraction vertex had to pass a χ^2 cut and all outgoing tracks had to have a first observed hit consistent with the particle originating from the reconstructed vertex. Candidate vertices with two outgoing tracks and kinematically compatible with the decay of a K_S^0 or Λ produced in the interaction region were not considered.

A search was then performed for the incoming particle which caused the interaction. Tracks which had been reconstructed in only the VD or the VD and ID were extrapolated to the candidate nuclear reinteraction vertex, and associated to the vertex if consistency was found. This prevented double counting of VD-ID tracks and reconstructed nuclear reinteractions. If there was no such track the momentum and charge of the incoming hadron were estimated from the sum over the outgoing particles associated to the vertex. For τ decays it is a good approximation to assume all such nuclear reinteraction vertices are caused by charged particles, as K^0 mesons are the only source of neutral hadrons producing nuclear reinteractions and are infrequently produced.

In simulation, the algorithm was $(82.4\pm0.2)\%$ efficient in 1-prong τ decays for incoming particle momenta above 1 GeV/c, and $(83.2\pm0.4)\%$ efficient in 3-prong τ decays. The efficiency had little dependence on the τ decay multiplicity or on the charged secondary particle multiplicity in the nuclear reinteraction. The position of the reinteraction vertex was reconstructed with a precision of better than 1 mm in three dimensions.

In a similar manner as for the converted photons, the reconstructed and unreconstructed nuclear reinteractions were studied as a function of the reinteraction radius. The rates of reconstructed nuclear reinteractions were obtained from the $\tau^+\tau^-$ sample in data and simulation. The radial distribution of reconstructed hadronic reinteractions is shown in Fig. 7. Some localised discrepancies, more marked than in the case of the photon conversions, are visible in the detailed description of the ID trigger layers and TPC in the simulation. The flat tail for radii
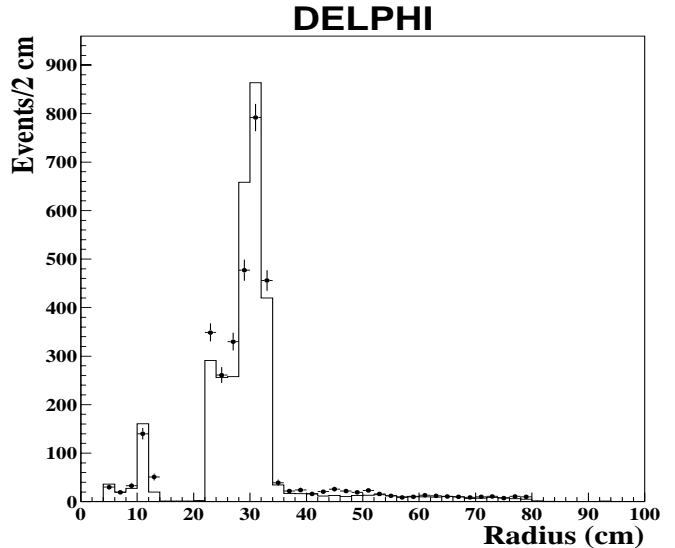

Fig. 7. Distribution in $e^+e^- \to \tau^+\tau^-$ events of reconstructed radius of the inelastic nuclear reinteractions. Data are dots, the line is simulation after applying correction factors

greater than 35 cm is due to reinteractions in the TPC cathode plane at $\theta \approx 90°$.

The unreconstructed nuclear reinteractions were measured by studying the multiplicity distribution for charged particle tracks with impact parameters in the r-ϕ plane greater than 1.5 cm in the hemisphere opposite a well reconstructed leptonic τ decay candidate. Simulation studies showed that this was dominated by τ decays with an unreconstructed nuclear reinteraction for multiplicities of four and greater. The τ decay hemispheres used to estimate this effect had to have no reconstructed nuclear reinteraction. This removed the risk of a false measurement arising from potential discrepancies in the charged particle multiplicity due to data/simulation differences in the track inclusion efficiency of the nuclear reinteraction reconstruction algorithm. The reinteraction radius was taken as the radius of the material surface lying immediately inside the first measured point on any of the charged particle tracks with a high impact parameter.

The measured correction factors A_{rec}^{nucl} and A_{unrec}^{nucl}, analogous to the quantities A_{rec}^{conv} and A_{unrec}^{conv} for conversions, are given in Table 2, together with the data/ simulation ratio of the efficiencies for reconstruction of inelastic nuclear reinteractions $\epsilon_d^{nucl}/\epsilon_s^{nucl}$ and the derived data/simulation ratio of material in terms of nuclear interaction lengths X_d^{nucl}/X_s^{nucl}. The region of the ID jet chamber gas volume, (13 cm to 22 cm) has been included together with the region at lower radius as it has a very small number of nuclear interaction lengths, of order 10^{-4}. These results indicate that for nuclear interactions the material at lower radii than the TPC gas volume is overestimated by about 9% in the simulation program while the reconstruction efficiency is consistent in data and simulation. There is a significant difference in the estimated data/simulation material ratios for nuclear and electromagnetic interactions. This can be attributed to the com-

Table 2. Factors used to correct simulated nuclear reinteractions for data/simulation discrepancies as a function of the radius of the reinteraction point. Column 5 shows the data/simulation ratio of reconstruction efficiency and column 6 the equivalent ratio for the material

Radius		Inelastic nuclear reinteractions			
Lower	Upper	A_{rec}^{nucl}	A_{unrec}^{nucl}	$\epsilon_d^{nucl}/\epsilon_s^{nucl}$	X_d^{nucl}/X_s^{nucl}
0cm	22.0cm	0.91±0.08	1.01±0.02	0.95±0.05	0.96±0.04
22.0cm	28.5cm	0.93±0.04	1.36±0.15	0.96±0.13	0.97±0.04
28.5cm	50cm	0.86±0.03	1.00±0.03	0.98±0.03	0.87±0.03
0cm	50cm	0.89±0.02	1.01±0.02	0.98±0.02	0.91±0.02

plexity of the composite material structure together with the means by which each of these quantities is introduced in the simulation program, as well as to possible weaknesses in the modelling of the hadronic reinteractions in the simulation program. The same effects are observed in $e^+e^- \to q\bar{q}$ events. The uncertainty in the initial production rate of hadrons in τ decays is relatively small and does not give an important systematic uncertainty in the measurement of A_{rec}^{nucl} and A_{unrec}^{nucl}.

As for the photon conversions, the nuclear reinteractions were studied for each year separately, particularly before and after the upgrade of the ID trigger layer in 1995.

Simulation studies indicate that the probability of reconstructing a fake nuclear reinteraction from τ decay secondary particles where none was present was 5×10^{-4} in 3-prong τ decays. However most such events were still classified as 3-prongs. The associated uncertainty was taken to be 100% of the size of the effect. The probability of reconstructing a fake nuclear reinteraction from a K_S^0 decay was negligible.

The probability that a hadron produced in a τ decay would undergo an elastic nuclear reinteraction before the TPC sensitive volume was estimated from simulation to be $(3.29\pm0.05)\%$. The typical signature of such an interaction was a charged particle track with a kink at the scattering point in the detector material. For large scatters the reconstruction algorithm would not reconstuct one but two tracks, one before and one after the scatter. This led typically to a signature of one VD-ID track and one TPC-OD track, and did not alter the observed track multiplicity in the TPC and OD.

5.4 Topology selection criteria

By judicious application of the VD hits requirement, and taking into account that the τ must decay into an odd number of charged particles, algorithms were constructed to minimise the sensitivity to the VD association efficiency and the knowledge of the material reinteractions; these are described below. In the following a "good" track is defined as a charged particle track which has associated TPC or OD hits and is not identified as originating from a conversion or nuclear reinteraction in the detector material. For simplicity, the VD-ID track classification, in addition to including tracks reconstructed using only the VD and ID detectors, includes tracks reconstructed as the ingoing charged hadron to a nuclear reinteraction. In τ decay hemispheres where the presence of a converted photon was signalled by the electron identification algorithm, the observed number of good tracks was reduced by two (or by one in the rare case of an even number of good tracks) for the purposes of the topology classification.

Individual τ decay hemispheres were allotted to five different classes dependent on the number of reconstructed tracks in the TPC, VD, etc. The first three of these classes correspond closely to events with clean reconstruction of a 1-prong, 3-prong or 5-prong topology. The other two classes contain the small number of τ decay hemispheres where there was more ambiguity in the reconstruction of the topology, but where some discrimination was still possible.

A 1-prong τ decay was defined as a τ decay hemisphere satisfying any of the following criteria:

- only one good track with associated VD hits, and no other tracks with associated VD hits;
- only one good track, without VD or ID hits, and one VD-ID track;
- no good tracks, and only one VD-ID track.

3-prong τ decays were isolated by demanding τ decay hemispheres satisfying at least one of the following sets of criteria:

- three, four or five good tracks, of which either two or three had VD hits;
- two good tracks with associated VD hits, plus one VD-ID track;
- one good track with associated VD hits, plus one or two VD-ID tracks pointing within 3° in azimuth of a TPC sector boundary.

Candidate 5-prong τ decays were selected if they satisfied at least one of the following topological criteria:

- five good tracks of which at least four had two or more associated VD hits;
- four good tracks with VD hits, and one other VD-ID track.

Additional criteria were applied in the selection of 5-prong τ decays due to the large potential background from hadronic Z decays and mis-reconstructed 3-prong τ decays. The background originating from $\nu_\tau 3h^\pm \geq 1\pi^0$ final states with a Dalitz decay was expected to occur at a

Table 3. Estimates of the selection and topology classification efficiencies, in percent, for different exclusive decay modes, as obtained from simulation. The efficiencies are corrected for observed discrepancies between data and simulation in the rate and reconstruction efficiency of material reinteractions. The quoted uncertainties are from the simulation statistics only

true τ decay mode	$\tau^+\tau^-$ selection	Topology Classification				
		1	3	5	$1'$	$3'$
$e^-\bar{\nu}_e\nu_\tau$	50.60±0.07	99.95±0.00	0.00±0.00	0.00±0.00	0.02±0.00	0.02±0.00
$\mu^-\bar{\nu}_\tau\nu_\mu$	53.31±0.07	99.96±0.00	0.00±0.00	0.00±0.00	0.01±0.00	0.03±0.00
$\pi^-\nu_\tau$	49.69±0.09	99.88±0.01	0.04±0.01	0.00±0.00	0.00±0.00	0.08±0.01
$\pi^-\pi^0\nu_\tau$	51.77±0.06	97.87±0.03	0.60±0.01	0.00±0.00	0.84±0.02	0.69±0.01
$\pi^-2\pi^0\nu_\tau$	51.07±0.11	95.88±0.06	1.25±0.03	0.00±0.00	1.42±0.04	1.45±0.04
$\pi^-3\pi^0\nu_\tau$	48.89±0.25	94.36±0.16	1.68±0.09	0.00±0.00	1.83±0.10	2.13±0.10
$K^-\nu_\tau$	49.43±0.36	99.90±0.03	0.02±0.02	0.00±0.00	0.01±0.01	0.06±0.03
$K^-\pi^0\nu_\tau$	51.40±0.47	97.66±0.20	0.85±0.12	0.00±0.00	0.80±0.12	0.69±0.11
$K^-2\pi^0\nu_\tau$	50.42±1.12	94.65±0.71	2.28±0.47	0.00±0.00	1.39±0.37	1.68±0.40
$\pi^-K^0_L\nu_\tau$	53.10±0.48	99.79±0.06	0.07±0.03	0.00±0.00	0.00±0.00	0.14±0.05
$\pi^-K^0_L\pi^0\nu_\tau$	51.85±0.73	97.32±0.33	0.78±0.18	0.00±0.00	0.78±0.18	1.11±0.21
$K^-K^0_L\nu_\tau$	54.60±0.87	99.78±0.11	0.11±0.08	0.00±0.00	0.00±0.00	0.11±0.08
$K^-K^0_L\pi^0\nu_\tau$	52.66±1.24	96.71±0.61	0.94±0.33	0.00±0.00	0.94±0.33	1.41±0.40
$\pi^-K^0_LK^0\nu_\tau$	52.82±1.04	95.12±0.62	3.72±0.54	0.00±0.00	0.08±0.08	1.07±0.30
$\pi^-K^0_S\nu_\tau$	52.17±0.48	94.48±0.30	4.30±0.27	0.00±0.00	0.16±0.05	1.06±0.14
$\pi^-K^0_S\pi^0\nu_\tau$	50.78±0.73	92.64±0.54	4.65±0.43	0.00±0.00	0.55±0.15	2.16±0.30
$K^-K^0_S\nu_\tau$	52.38±0.86	94.50±0.54	4.42±0.49	0.00±0.00	0.06±0.06	1.02±0.24
$K^-K^0_S\pi^0\nu_\tau$	51.32±1.32	92.56±0.97	5.01±0.80	0.00±0.00	0.41±0.23	2.03±0.52
$\pi^-2K^0_S\nu_\tau$	46.34±1.80	86.72±1.80	10.45±1.63	0.00±0.00	0.00±0.00	2.82±0.88
1-prong	51.42±0.03	98.71±0.01	0.42±0.01	0.00±0.00	0.44±0.01	0.43±0.01
$2\pi^-\pi^+\nu_\tau$	54.71±0.11	0.90±0.03	90.26±0.09	0.01±0.00	2.10±0.04	6.74±0.07
$2\pi^-\pi^+\pi^0\nu_\tau$	53.88±0.13	1.26±0.04	86.39±0.12	0.10±0.01	3.15±0.06	9.10±0.10
$3\pi^\pm2\pi^0\nu_\tau$	53.14±0.46	1.37±0.15	83.64±0.46	0.22±0.06	3.68±0.24	11.09±0.39
$3\pi^\pm3\pi^0\nu_\tau$	52.13±1.06	1.46±0.35	78.73±1.20	0.17±0.12	4.74±0.62	14.90±1.05
$K^-\pi^-\pi^+\nu_\tau$	54.64±0.56	1.03±0.15	90.35±0.45	0.00±0.00	1.70±0.20	6.92±0.38
$K^-K^+\pi^+\nu_\tau$	53.87±0.90	2.08±0.35	87.23±0.82	0.00±0.00	1.10±0.26	9.59±0.73
3-prong	54.32±0.08	1.06±0.02	88.51±0.07	0.05±0.00	2.54±0.03	7.84±0.06
$3\pi^-2\pi^+\nu_\tau$	49.63±1.19	0.11±0.11	12.63±1.13	57.52±1.67	0.23±0.16	29.51±1.55
$5\pi^\pm\pi^0\nu_\tau$	48.91±2.23	0.00±0.00	15.04±2.28	52.85±3.18	0.81±0.57	31.30±2.96
5-prong	49.47±1.05	0.09±0.09	13.16±1.01	56.49±1.48	0.36±0.18	29.90±1.37

similar level to the signal. The electron rejection criteria described in Sect. 5.2 reduced this background by about 70%, and it was further suppressed by requiring that all good tracks had a momentum greater than 1 GeV/c. To reject $Z \to q\bar{q}$ events it was required that the total momentum of the 5-prong system be greater than 20 GeV/c. Only good tracks were included in the calculation of this quantity.

These three classes accounted for 97.6% of candidate τ decays in the $\tau^+\tau^-$ sample. The remaining 2.4% of candidate τ decays were mostly 1-prong and 3-prong τ decays with some pattern recognition failure or detector inefficiency. These were classified into two categories, $1'$ and $3'$, corresponding to 1-prong and 3-prong τ decays respectively. Candidate τ decay hemispheres of type $1'$ had to satisfy at least one of the following criteria:

– one good track, with associated VD hits, plus two VD-ID tracks not pointing within 3° in azimuth of a TPC sector boundary;
– one good track, plus a conversion candidate selected with the electron identification algorithm.

The $3'$ category contained all other τ decay hemispheres failing to pass any of the previous classification requirements. In particular it contained those events with either four or five good tracks of which either four or more had associated VD hits, but not satisfying the 5-prong class requirements. This criteria had a higher efficiency for 5-prong decays than for 3-prong decays, but due to the much greater 3-prong branching ratio the $3'$ category was dominated by 3-prong decays. Table 3 contains the efficiencies of these selection requirements for the different exclusive τ decay modes and the inclusive single-hemisphere topological selections, as obtained from simulation and after

Table 4. Fractional non-$\tau^+\tau^-$ backgrounds (in %) in the $\tau^+\tau^-$ sample and the different event topology classes. The classes 1'-5 and 3'-5 have very small populations and the estimated background is zero due to statistical fluctuations in the simulation

Source of Background	All Topologies	Event Topology													
		1-1	1-1'	1-3	1-3'	1-5	1'-1'	1'-3	1'-3'	1'-5	3-3	3-3'	3-5	3'-3'	3'-5
$\mu^+\mu^-$	0.11±0.01	0.19	0.06	0.00	0.07	0.00	0.00	0.00	0.00	0.00	0.00	0.00	0.00	0.00	0.00
e^+e^-	0.40±0.07	0.65	0.00	0.01	0.00	0.00	0.00	0.00	0.00	0.00	0.00	0.00	0.00	0.00	0.00
$q\bar{q}$	0.29±0.01	0.03	0.00	0.32	3.39	1.01	0.00	1.16	0.00	0.00	1.61	14.8	21.2	77.0	0.00
$e^+e^-e^+e^-$	0.27±0.03	0.49	0.00	0.00	0.00	0.00	0.00	0.00	0.00	0.00	0.00	0.00	0.00	0.00	0.00
$e^+e^-\mu^+\mu^-$	0.10±0.01	0.16	0.00	0.01	0.00	0.00	0.00	0.00	0.00	0.00	0.00	0.33	0.00	0.00	0.00
$e^+e^-\tau^+\tau^-$	0.27±0.03	0.35	3.91	0.23	0.76	0.00	21.1	0.97	2.88	0.00	0.20	0.60	0.00	0.45	0.00
$e^+e^-q\bar{q}$	0.02±0.01	0.03	0.00	0.03	0.44	0.00	0.00	0.00	0.00	0.00	0.00	0.00	0.00	0.00	0.00
cosmic rays	0.05±0.01	0.07	0.01	0.00	0.00	0.00	0.00	0.00	0.00	0.00	0.00	0.00	0.00	0.00	0.00
Total	1.51±0.10	1.97	3.98	0.60	4.66	1.01	21.1	2.13	2.88	0.00	1.81	15.7	21.2	77.4	0.00

corrections for observed discrepancies between data and simulation in the rate and reconstruction efficiency of material reinteractions.

Events were classified according to both the hemisphere classifications into 14 event topology classes: 1-1, 1-1', 1-3, 1-3', 1-5, 1'-1', 1'-3, 1'-3', 1'-5, 3-3, 3-3', 3-5, 3'-3' and 3'-5. The class 5-5 was not included as these events were removed by the multiplicity cut in the $\tau^+\tau^-$ preselection and in any case would give a negligible signal contribution. The selection of event classes up to multiplicity five assumes that the inclusive branching ratio of the τ to seven charged particles is negligible. While inclusion of higher multiplicity classes is possible, the DELPHI sample size is insufficient to reach the level of precision obtained by CLEO [16].

The various sources of non-$\tau^+\tau^-$ background are detailed in Table 4 for each of the event topology classes.

6 The fit and systematics

6.1 Fitting procedure

A reweighting technique was used to take into account the observed data/simulation discrepancies in the rates and reconstruction efficiencies of nuclear reinteractions, photon conversions and δ-rays. Each secondary or tertiary particle i in a simulated $\tau^+\tau^-$ event k was given a weight W_i^{part}. For particles interacting with the detector material this weight was obtained from the studies described in Sect. 5 and summarised in Tables 1 and 2. These weights were a function of the radius and type of the reinteraction, as follows:

- reconstructed converted photons:
  $W_i^{part} = A_{rec}^{conv}(\mathrm{r})$;
- unreconstructed converted photons:
  $W_i^{part} = A_{unrec}^{conv}(\mathrm{r})$;
- reconstructed inelastic nuclear reinteractions:
  $W_i^{part} = A_{rec}^{nucl}(\mathrm{r})$;
- unreconstructed inelastic nuclear reinteractions:
  $W_i^{part} = A_{unrec}^{nucl}(\mathrm{r})$;

- δ-rays: $W_i^{part} = X_d^{EM}/X_s^{EM}(\mathrm{r})$;
- bremsstrahlung emitting electrons:
  $W_i^{part} = X_d^{EM}/X_s^{EM}(\mathrm{r})$;
- elastic nuclear reinteractions:
  $W_i^{part} = X_d^{nucl}/X_s^{nucl}(\mathrm{r})$.

It was also necessary to reweight particles which did not reinteract so as to maintain the internal normalisation of the simulation sample with respect to parameters such as angular distributions, momentum distributions, or the τ exclusive branching ratios. Failure to achieve this could lead to biases within the simulation sample as a function of photon multiplicities, charged hadron multiplicities, angular regions with different amounts of material, or could bias the preselection of the $\tau^+\tau^-$ sample with respect to certain types of decay mode. Non-interacting photons were given a weight W_i^{part} given by

$$W_i^{part} = \frac{N^\gamma - \sum\limits_{j\in\mathrm{int.photons}} W_j^{part}}{N^\gamma - N_{int}^\gamma}, \qquad (8)$$

where N^γ is the total number of photons produced by τ decays or by interactions with material of τ decay products in the simulation sample. N_{int}^γ is the number of photons with a material reinteraction. The sum is over all photons with a material reinteraction. To maintain the angular and momentum distributions the above weight calculation was performed separately for individual bins in a three-dimensional space of the photon polar angle, azimuthal angle and momentum. A similar procedure was used to reweight non-interacting hadrons, particles not emitting a δ-ray (a very small correction) and electrons without any bremsstrahlung emission.

With every secondary and tertiary particle i in a simulated event k given a weight W_i^{part}, the weight W_k^{event} of the event was given by the product of all these weights:

$$W_k^{event} = \prod_{i\in k} W_i^{part}. \qquad (9)$$

The numbers of selected events in each event topology class are shown in Table 5. A maximum likelihood fit

Table 5. The second and third columns contain the number of observed events in each class and number predicted from the maximum likelihood fit of the τ topological branching ratios. The fourth column contains the χ^2 contribution for each class to the overall χ^2

Class	Observed	Fit Output	χ^2
$1-1$	56219	56149.0	0.1
$1-1'$	858	871.0	0.2
$1-3$	18681	18813.5	0.9
$1-3'$	2350	2331.5	0.1
$1-5$	94	95.6	0.0
$1'-1'$	4	3.9	0.0
$1'-3$	131	134.8	0.1
$1'-3'$	16	14.7	0.1
$1'-5$	0	1.2	1.2
$3-3$	1481	1451.5	0.6
$3-3'$	409	357.4	7.4
$3-5$	17	13.8	0.7
$3'-3'$	76	97.7	4.8
$3'-5$	1	1.5	0.2
All	80337	80337.1	16.4

assuming Poissonian probabilities was performed to the reweighted numbers of events estimated using (3). The number of $\tau^+\tau^-$ events ($N_{\tau\tau}$ in (3)) and the branching ratios B_1 and B_5 were allowed to vary in the fit while B_3 was constrained by the relation $B_1+B_3+B_5 = 1$. The output of the fit is also shown in Table 5. The results of this fit were: $B_1 = (85.316\pm0.093)\%$; $B_3 = (14.569\pm0.093)\%$; $B_5 = (0.115 \pm 0.013)\%$, where only the statistical error from the fit is quoted. An estimate of the consistency of the fit was made by calculating a χ^2. This took into account only the statistical uncertainties. It gave a $\chi^2/\text{n.d.f.}$ of 16.4/11, indicating good consistency. The contribution to the χ^2 from each class is shown in Table 5.

6.2 Systematics

In general, the systematic uncertainties on the topological branching ratios due to any particular effect were estimated simultaneously for B_1, B_3 and B_5 by repeating the analysis, including the $\tau^+\tau^-$ preselection, after modifying the relevant variable in the simulation. This accounted for correlations in the systematic uncertainties between the different branching ratios and correlations in efficiencies and backgrounds between the different event classes and the $\tau^+\tau^-$ preselection.

6.2.1 Preselection

The main systematic effects of the $\tau^+\tau^-$ selection criteria on the result can arise through the mis-calibration of the quantities used in the selection. These quantities can be classified into cuts related to energy or momentum measurements, such as E_{rad}, p_{rad} and E_{vis}, or those cuts related to multiplicity, such as the isolation angle, which can be incorrectly estimated if extra secondary particles are produced in reinteractions with detector material. This second effect is taken account of by the systematics in the reweighting of the secondary interactions, discussed in Sect. 6.2.3. A separate systematic uncertainty is included for the energy and momentum scales below. Other effects such as tracking efficiency, trigger efficiency and uncertainties on the τ exclusive branching ratios can have an effect on the $\tau^+\tau^-$ preselection efficiency. These sources of systematic uncertainty are discussed below, and in general the systematic uncertainties on the topological branching ratios take into account effects in the preselection.

Any remnant discrepancies due to $\tau^+\tau^-$ preselection criteria were checked by studying the agreement between data and simulation for the distributions of the $\tau^+\tau^-$ selection variable for each of the different event topology classes. With the corrections to the background levels discussed in Sects. 4.2 and 5, good agreement was found, in particular in the regions of the cuts.

The uncertainties due to the backgrounds from non-$\tau^+\tau^-$ sources were estimated by varying the background normalisations by their uncertainties obtained as described in Sect. 4, and are listed in Table 6. The distribution of the neural network variable used for $q\bar{q}$ rejection (see Fig. 2) displays a 15% excess in the data compared with simulation in the region [0.05;0.8] of the output neuron distribution. This region was dominated by $\tau^+\tau^-$ events and was studied to see if there were any discrepancies in the input variables, and by checking the multiplicity distributions of the events. No discrepancies were found. The systematic uncertainty was estimated by rescaling the numbers of rejected signal events in all classes by 15%.

6.2.2 Tracking

Within the angular acceptance of this analysis, there are four tracking detectors which can contribute to the track reconstruction of all charged particles: the VD, ID, TPC and OD. The reconstruction of "good" tracks is strongly dependent on the TPC with its full three-dimensional readout. The redundancy in the track reconstruction obtained by the inclusion of τ decay hemispheres with only a VD-ID track in the $\tau^+\tau^-$ sample and 1-prong subsample reduces greatly the sensitivity of the measurement to inefficiencies within a given subdetector, and allows direct cross-checks to be made.

In simulation, for non-interacting particles, the efficiency for the TPC to reconstruct an isolated charged particle which passes through a sensitive gas volume far from dead regions is 99.95%. However, even with the redundancy of the different tracking subdetector components in DELPHI, to measure this in data directly is difficult because of material reinteractions between different subdetectors which can cause the particle to be lost before entering the TPC sensitive volume. These effects tend to reduce the measured efficiency. For the data, the efficiency

of the TPC in its sensitive regions was estimated using the redundancy of the tracking system to be $(99.35 \pm 0.05)\%$. The identical procedure was applied to the simulation, yielding an efficiency of $(99.31 \pm 0.01)\%$, in excellent agreement with the data, and implying that the modelling of the TPC efficiency in the simulation was accurate. The true inefficiency in simulation is a factor of 12 lower than the inefficiency estimated by this method. The uncertainty on the TPC reconstruction efficiency in the TPC sensitive region was taken conservatively to be 0.05% to account for any systematic effects in its estimation.

The TPC efficiency for isolated tracks in the sector boundary region was studied using inclusive low multiplicity events but excluding the $\tau^+\tau^-$ events. This sample consists of radiative dilepton events and the high energy part of the two-photon leptonic event spectrum. The number of reconstructed tracks in the TPC boundary region was compared to that expected by normalisation of the sensitive region of the TPC sectors, in bins of momentum. The loss of tracks was compatible with zero below about 5 GeV/c, rising to 3.5% at 45 GeV/c. Data and simulation agree well in their behaviour. The inefficiency estimated from data for the $\tau^+\tau^-$ momentum distribution was $(2.73 \pm 0.04)\%$, compatible with the result in simulated $\tau^+\tau^-$ events. The TPC efficiency was varied by throwing away tracks containing TPC hits in simulation and repeating the analysis, including the $\tau^+\tau^-$ preselection stage. The error was scaled by a factor two to account for any systematic effects in the procedure.

The attachment of VD hits to a track is the main criterion used in this analysis to determine the multiplicity of a τ decay. The association efficiency and misassociation probability of a VD hit to be attached to a charged particle track has been studied [20] on large samples of $e^+e^- \to q\bar{q}$ events, and on isolated topologies such as $\mu^+\mu^-$ final states. These studies indicate that the efficiency in simulation and data agree to within $\pm 2\%$. The associated systematic uncertainties were obtained from the shifts in the results observed when randomly removing 2% of associated VD hits and repeating the analysis, including the $\tau^+\tau^-$ preselection stage.

Within the τ sample itself the rate of association of different subdetectors to a reconstructed charged particle track was studied for different τ decay topologies. In candidate 1-prong decays, the hit association probabilities for the VD, ID and OD were studied for tracks which had an associated TPC track segment. The probabilities obtained in data and simulation were compared and the relative differences calculated. These differences were 0.0% for the VD, $+2.3\%$ for the ID and -1.2% for the OD. The equivalent numbers for 3-prong decays were -0.7%, $+2.5\%$ and $+0.6\%$ respectively. The results for the ID were unchanged if in addition the VD was required to be associated to a track, and vice-versa. The small fraction of tracks without a TPC track segment showed a level of agreement for the proportions of tracks with different subdetectors which was better than 3% in all cases.

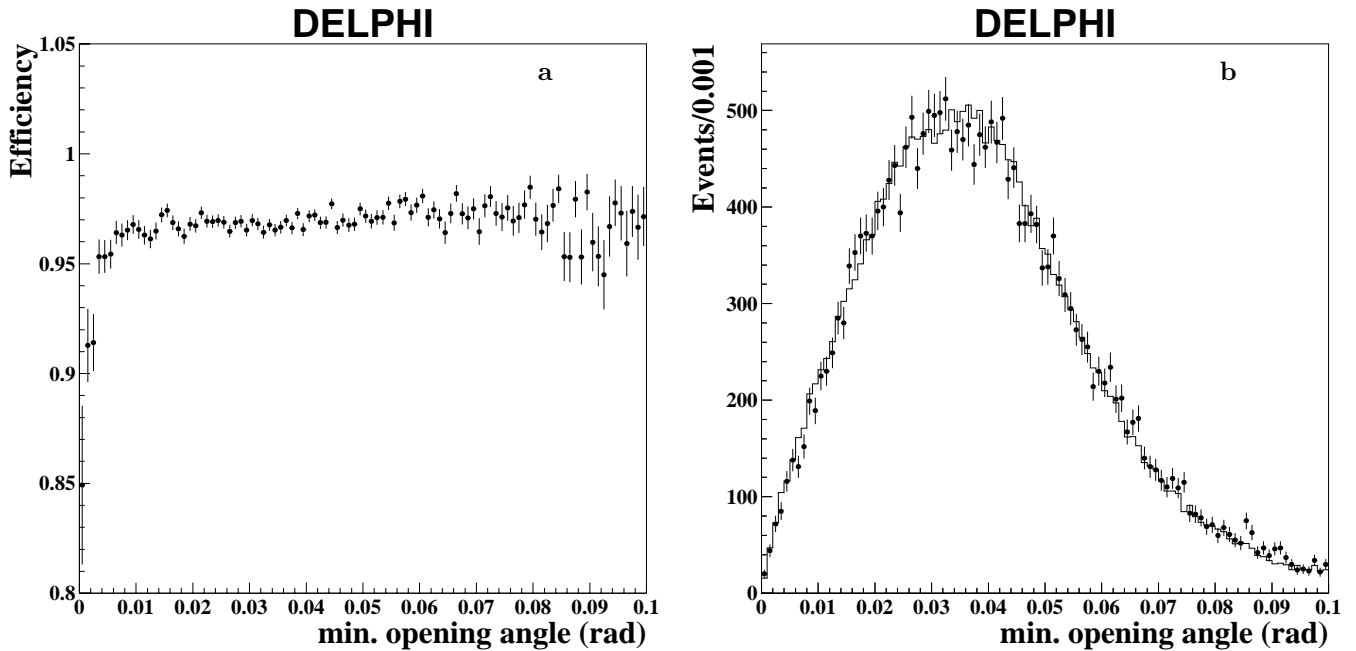In simulation, the preselection efficiency was found to be independent of the combination of the subdetectors attached to a track at a level below 0.1%. Given the observed discrepancies between data and simulation, any effect on the preselection efficiency due to this source was $\mathcal{O}(10^{-5})$. The uncertainties arising from the probability of including an ID hit on a track were estimated to be 2.2×10^{-5} for both B_1 and B_3 with a full anticorrelation and has been included in the tracking systematic uncertainty. The analogous uncertainty for the OD was negligible.

It was observed that the level of Bhabha background was correlated with the existence of an OD hit on a track. This was due to bremsstrahlung, and resolution effects in the p_{rad} variable. The level of agreement observed between the data and the simulation implied that the Bhabha background was consistent with the estimation made in Sect. 4.2.

The two-track resolution has been studied by data-simulation comparison of the minimum opening angle in three dimensions between tracks in τ decay hemispheres with more than one track. Figure 8a shows the efficiency in simulation to reconstruct a 3-prong τ decay as a function of the minimum opening angle. It is flat within 1% except for a fall-off of about 5% in reconstruction efficiency for a minimum opening angle below 3 mrad. As is visible in the distribution of the minimum opening angle in candidate 3-prong τ decays shown in Fig. 8b, less than 1% of 3-prong τ decays lie in this region and data and simulation are compatible within the statistical precision. A systematic uncertainty was attributed to the two-track resolution by varying the efficiency in the region with minimum opening angle below 3 mrad by the uncertainty allowed from the statistical uncertainty of the data. There was no observable fall-off in efficiency for low values of the minimum differences between the azimuthal or polar angles of tracks in a 3-prong hemisphere. The minimum opening angle distribution in candidate 5-prong τ decays is shown in Fig. 9.

The association efficiency of the TPC in 3-prong τ decays and its dependence on the minimum opening angle were studied by comparing the rate of candidate τ decays containing three tracks with associated TPC hits with the rate of decays containing either two tracks with TPC hits plus one track without TPC hits or one track with TPC hits plus two tracks without TPC hits. Figure 10 shows the data over simulation ratio of the fraction of candidate 3-prong τ decays containing three tracks with associated TPC hits, as a function of the minimum opening angle. It shows compatibility with unity in all regions except for a small discrepancy of about $+3\%$ for minimum opening angles in the region of 4 to 7 mrad. The average of the ratio for all minimum opening angles is 1.0016 ± 0.0008, consistent with unity within two standard deviations. The difference from unity can be directly related to the efficiency for a charged particle track to have associated TPC hits in 3-prong τ decays. The uncertainties on the topological branching ratios were estimated by varying the probability in simulated 3-prong τ decays to have TPC hits associated to a track by 1.6×10^{-3} and repeating the analysis. The same procedure was carried out for 5-prong decays.

Figure 8b shows some differences between data and simulation in the region between 3 and 15 mrad, with

Fig. 8. a The selection efficiency in simulation for candidate 3-prong decays as a function of the minimum angle in three dimensions between any two charged particles. **b** The distribution of the minimum angle in three dimensions between any two charged particles in candidate 3-prong τ decays. Dots are data, line is simulation
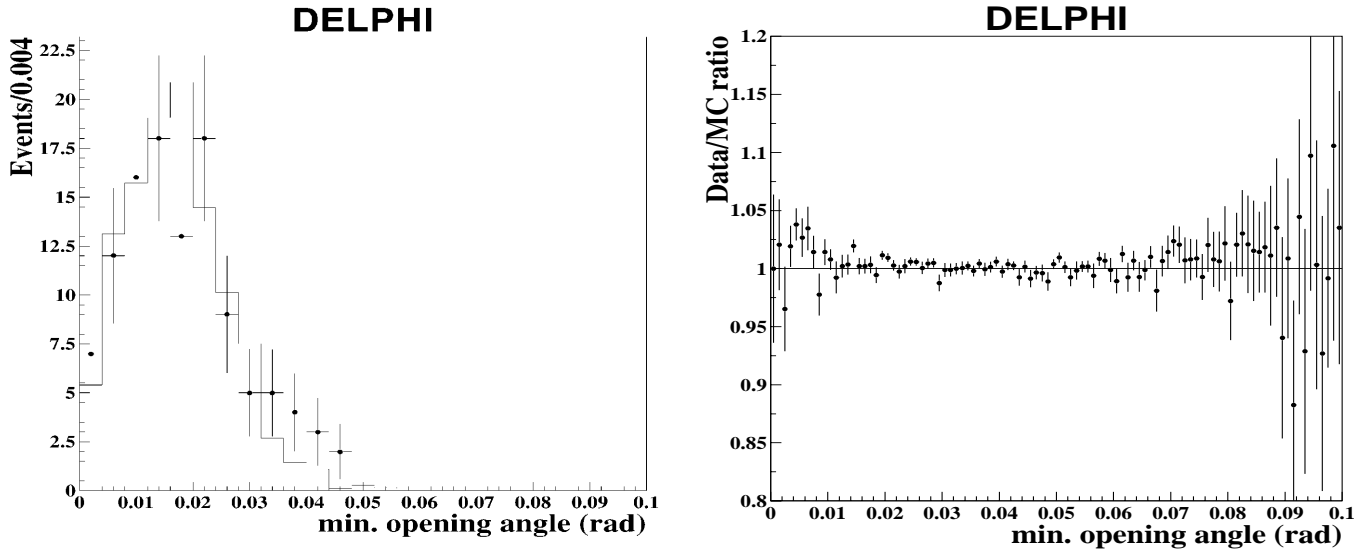
Fig. 9. The minimum angle in three dimensions between any two charged particles in candidate 5-prong τ decays. Dots are data, line is simulation

Fig. 10. For candidate 3-prong τ-decays, the ratio of data to simulation of the fraction of candidate decays where three tracks had associated TPC hits, as a function of the minimum opening angle

the simulation tending to lie slightly above the data. This can be due to the decay modelling, for which the attendant systematic uncertainties are discussed in Sect. 6.2.4. However track reconstruction effects cannot be excluded. While systematics in the TPC association efficiency are accounted for above, the deviation from unity of the ratio shown in Fig.10 can also give an estimate of the rate of track reconstruction without the TPC, in particular of VD-ID tracks. An upper estimate of the magnitude of

this effect for close tracks was derived by integrating up to 15 mrad the deviations from unity of this ratio times the number of events in a given bin of minimum opening angle. This procedure gave an uncertainty of 1.2×10^{-4} on B_3, together with uncertainties on B_1 and B_5 induced via the correlations in the fit. This accounted for potential differences between data and simulation in the VD-ID

track reconstruction in the small minimum opening angle region of 3-prong τ decays.

The reconstructed charge in a τ decay hemisphere was studied for different event and decay topologies. The charge was not used to classify τ decays or select $\tau^+\tau^-$ events, so this provided an indirect cross-check of the track reconstruction. Use was made of the constraint that the two τ-decay hemispheres arose from τ's of opposite charge. For events in the data belonging to the 1-1 event class, an estimated (99.88±0.01)% of τ decays had the charge correctly reconstructed. The rate in the simulation was (99.91±0.01)%. For 3-prong decays in data, (98.57±0.09)% had the correctly signed unit charge, compared with (98.60±0.03)% in simulation, while (0.54±0.06)% had a charge of three with the correct sign as compared with (0.52±0.02)% in simulation. The remainder had the wrongly signed charge. In 5-prong decays an estimated (90.5±0.7)% had the correctly reconstructed unit charge in data compared with (89.7±0.3)% in simulation.

6.2.3 Reinteractions and K_S^0 reconstruction

Uncertainties from the photon conversion reconstruction were estimated by varying by their uncertainties the correction factors for the reconstructed and unreconstructed conversions, given in Table 1, which were obtained from data test samples as described in Sect. 5.2. A contribution for the uncertainty in the incident photon rate in the dileptonic test samples was included. The resultant uncertainties are dominated by the contribution from the unreconstructed conversions. A similar approach was taken for the nuclear reinteractions. Here again the uncertainty arising from the unreconstructed nuclear reinteractions was the most significant contribution.

Both the photon conversion and hadronic reinteraction errors contain contributions to account for the uncertainty on the rate of fake reconstructions which cause the topology to be misidentified.

The 1-prong τ decay class has a number of different subclasses which cover the different reconstruction possibilities for an elastic nuclear reinteraction in a 1-prong hadronic τ decay. In simulation, of the 3.3% of hadrons in τ decays undergoing an elastic scatter before the TPC sensitive volume 99.4% were correctly attributed to the 1-prong class, leading to a classification inefficiency of 2.0×10^{-4} for 1-prong hadronic τ decays. A cross-check of the elastic scatters was performed using a kink algorithm which attempted to link up pairs of tracks consistent with both tracks having been produced by a single charged particle experiencing a large scatter in detector material. Comparison of the rates in data and simulation showed agreement within 20%, which was taken as a relative uncertainty on the effect. The effects of fake kink reconstructions by the algorithm had a negligible effect.

The uncertainty attributed to the electron identification had contributions from the uncertainties on the efficiencies for conversion rejection and for rejection of π^0

Dalitz decays, and from the probability of misidentifying a hadron as an electron. The study of the electron identification algorithm and its systematic uncertainties is described in Sect. 5.2.

The δ-ray rate is proportional to the mean atomic number Z of the material, while the factors which are applied correct for the number of radiation lengths, which is approximately proportional to the mean Z^2. This gives an ambiguity in the correction for δ-rays depending on whether it is due to the wrong mean Z, or to the wrong quantity of material, but with the correct mean Z. The correction factor used in the analysis, X_d^{EM}/X_s^{EM}, assumes the latter case. The former case would imply a factor of $(X_d^{EM}/X_s^{EM})^{1/2}$. This was applied and the observed variations on the branching ratios taken as systematic uncertainties.

Only the fraction ($\approx$5%) of $K_S^0 \to \pi^+\pi^-$ decays occuring inside the VD, and which the K_S^0 reconstruction algorithm failed to identify, gave fake charged primary τ decay products and hence the incorrect topology assignment. For the region inside the outer layer of the VD, the rate of successfully reconstructed K_S^0's was 0.91 ± 0.09 times the simulation prediction, showing good consistency. The quoted error is purely statistical. By comparison of data and simulation for candidate K_S^0 mesons reconstructed as decaying beyond the VD, the reconstruction efficiency and relative rate of photon conversions misidentified as K_S^0 were estimated to agree within 15%. The K_S^0 reconstruction algorithm can reconstruct a fake K_S^0 from two primary τ decay particles thus reducing the τ decay charged multiplicity by two. Simulation studies indicate that the scale of this effect was 5×10^{-5} of the 3-prong rate. The related systematic uncertainty was taken to be equal to the size of the effect.

6.2.4 Exclusive branching ratios and τ decay modelling

The exclusive branching ratios were varied within the uncertainties quoted in the Particle Data Listings [5]. To take account of any hidden correlations the quoted uncertainties have been scaled up by a factor of 1.5. The largest single contribution is from the decay mode $3\pi^\pm3\pi^0\nu_\tau$ with a high π^0 multiplicity and a large relative uncertainty on the branching ratio. The uncertainty also included a small contribution due to the decay modes $\tau^- \to K^-\pi^-\pi^+\pi^0\nu_\tau$ and $\tau^- \to K^-K^+\pi^-\pi^0\nu_\tau$ which were not included in the simulation.

The uncertainties associated with the modelling of the 3- and 5-prong decays were estimated by correcting the efficiencies taking into account differences between data and simulated invariant mass distributions. In addition, the hadronic structure of the 3π final state was varied between the default TAUOLA [15] model and that obtained in the DELPHI analysis of the 3π structure in τ decays [23]. For the $3\pi\pi^0$ structure the parameterisation of Model 1 of [24] was used and, as a cross-check, the parameterisation of $3\pi\pi^0$ used in [23] was used to reweight the distributions of the minimum opening angle.

6.2.5 Trigger, energy scale, τ polarisation and simulation statistics

The trigger efficiency for $\tau^+\tau^-$ final states was $(99.98 \pm 0.01)\%$ for events within the polar angle acceptance. Studies indicated that the inefficiency was due to events where both τ's decayed via the $\tau \to \mu\nu\nu$ mode [17]. It was assumed that the full inefficiency of $(2 \pm 1) \times 10^{-4}$ was contained in the 1-1 event class and the efficiency of this class and of the $\tau^+\tau^-$ preselection were modified accordingly. The associated systematic uncertainty was obtained by varying the inefficiency by its error.

The energy and momentum scales and resolution can affect many of the quantities used in the analysis, such as the $\tau^+\tau^-$ selection variables, invariant masses or the thrust (used in the q$\bar{\text{q}}$ rejection). The momentum scale was varied by 0.2%, the electron energy by 0.5% and the neutral electromagnetic energy by 0.2%. These variations were obtained in a study carried out for the τ polarisation measurement [25]. The associated systematic uncertainty on the topological branching ratio results was small.

The 1-prong selection efficiency has a slight sensitivity to the average τ polarisation because of acceptance effects in $\tau \to \pi\nu_\tau, K\nu_\tau$ decays due to the p_{rad} cut used in the $\tau^+\tau^-$ selection. The analysis used the result and uncertainty from the DELPHI analysis on τ polarisation [25].

The systematic uncertainty due to the limited simulation statistics was also included.

6.2.6 Other cross-checks and summary

A cross-check of the fitting procedure was performed by using the simulation itself as input to the fit; the results of the fit were compared with the input branching ratios and agreement was observed. This was repeated with different input branching ratios, again showing good agreement. The reweighting procedure was, where possible, cross-checked by direct calculation of the expected variation in the measured branching ratios when applying the weights for a given effect.

In the fit the main contributions to the χ^2 come from the 3-3′ and 3′-3′ classes. Both contain significant background from e$^+$e$^- \to$ q$\bar{\text{q}}$ events. Removing these two classes from the fit had an almost negligible effect on the results, within the bounds of expected statistical fluctuations. No systematic uncertainty was ascribed to this effect.

Other cross-checks were performed, including fitting the branching ratios hemisphere by hemisphere rather than event by event, using (2). For this fit it was practical to subdivide the sample even further into hemisphere subclasses dependent on the number of VD-ID-TPC(-OD) tracks, VD-ID tracks, number of conversions, nuclear reinteractions, etc. The branching ratios obtained with this approach were in excellent agreement with those obtained in the event-by-event fit.

Table 6. Contributions in units of 10^{-6} to the systematic uncertainties on B_1, B_3 and B_5. The uncertainties are signed to show the correlation between the different branching ratios. The 1-prong errors are always assumed positive

Source of systematic	1-prong	3-prong	5-prong
Dilepton background	110	−109	−1
Cosmic ray background	5	−5	<1
Four-fermion background	42	−41	−1
$Z \to$ q$\bar{\text{q}}$ background	25	−24	−1
Neural Network q$\bar{\text{q}}$ rejection	50	−48	−5
Tracking	157	−152	−16
VD efficiency	55	−60	+6
Conversions	126	−121	−8
Inelastic Nucl. reinteractions	90	−80	−10
Elastic Nucl. reinteractions	24	−24	−2
Electron identification	104	−97	−7
δ-ray weights	8	−8	<1
K_S^0 reconstruction	5	−5	<1
Exclusive BRs	228	−204	−44
3-prong decay modelling	116	−121	+10
Trigger	15	−15	<1
E and p scales	19	−20	+1
τ polarisation	18	−19	+1
Simulation statistics	310	−310	+31
Total systematic	492	477	59
Statistical	929	929	126

The fits were performed for each year's data separately. Good agreement was found for the results in the different years.

The different systematic uncertainties are summarised in Table 6. The systematic uncertainties are signed so as to give the correlation between the different branching ratios.

7 Conclusions

The measurements made of the 1, 3 and 5-prong topological branching ratios were

$$B_1 = (85.316 \pm 0.093_{stat} \pm 0.049_{sys})\%,$$
$$B_3 = (14.569 \pm 0.093_{stat} \pm 0.048_{sys})\%,$$
$$B_5 = (0.115 \pm 0.013_{stat} \pm 0.006_{sys})\%.$$

As expected in view of the small value of B_5, the branching ratios B_1 and B_3 are almost fully anti-correlated with a coefficient of -0.98. B_3 and B_5 have a correlation coefficient of -0.08, and B_1 and B_5 also have a correlation coefficient of -0.08. The B_1 and B_3 results are consistent with and slightly more precise than the results obtained in the PDG [5] combined fit to all τ decay data: $B_1 = (85.32 \pm 0.13)\%$; $B_3 = (14.58 \pm 0.13)\%$. The B_1 and B_3 results are more than twice as precise as the existing world averages [5] of $(84.59 \pm 0.33)\%$ and $(14.63 \pm 0.25)\%$ respectively. The results are in reasonable agreement with, but significantly

more precise than, the most recent direct measurements, by OPAL [26, 27], CLEO [28] and ALEPH [3].

The result on the 5-prong branching ratio is in good agreement with the world average of $(0.107 \pm 0.009)\%$ and the PDG best fit result of $(0.099 \pm 0.007)\%$ which include contributions from OPAL [29], CLEO [30] and ALEPH [4] measurements.

References

1. See discussion in Particle Data Group, R. Barnett et al., Phys. Rev. **D54** (1996) 1
2. CELLO Collab., H. J. Behrend et al., Z. Phys. **C46** (1990) 537
3. ALEPH Collab., D. Decamp et al., Z. Phys. **C54** (1992) 211
4. ALEPH Collab., D. Buskulic et al., Z. Phys. **C70** (1996) 579
5. Particle Data Group, D. E. Groom et al., Eur. Phys. J. **C15** (2000) 1
6. DELPHI Collab., P. Aarnio et al., Nucl. Instr. and Meth. **A303** (1991) 233
7. DELPHI Collab., P. Abreu et al., Nucl. Instr. and Meth. **A378** (1996) 57
8. S. Jadach et al., Comp. Phys. Comm. **79** (1994) 503; S. Jadach et al., Comp. Phys. Comm. **70** (1992) 69
9. J. E. Campagne, R. Zitoun, Z. Phys. **C43** (1989) 469
10. F. A. Berends, R. Kleiss, W. Hollik, Nucl. Phys. **B304** (1988) 712
11. S. Jadach et al., Phys. Lett. **B390** (1997) 298
12. T. Sjöstrand, Comp. Phys. Comm. **82** (1994) 74
13. F. A. Berends, P. H. Daverveldt, R. Kleiss, Phys. Lett. **B148** (1984) 489; Comp. Phys. Comm. **40** (1986) 271
14. T. Alderweireld et al., CERN Report CERN-2000-009 (2000) 219
15. S. Jadach et al., Comp. Phys. Commun. **76** (1993) 361
16. CLEO Collab., K. W. Edwards et al., Phys. Rev. **D56** (1997) R5297
17. DELPHI Collab., P. Abreu et al., Eur. Phys. J. **C10** (1999) 201
18. DELPHI Collab., P. Abreu et al., Eur. Phys. J. **C11** (1999) 383
19. DELPHI Collab., P. Abreu et al., Eur. Phys. J. **C16** (2000) 371
20. G. Borisov, C. Mariotti, Nucl. Inst. Meth. **A372** (1996) 181
21. DELPHI Collab., W. Adam et al., Z. Phys. **C69** (1996) 561
22. DELPHI Collab., P. Abreu et al., Phys. Lett. **B359** (1995) 411
23. DELPHI Collab., P. Abreu et al., Phys. Lett. **B426** (1998) 411
24. CLEO Collab., K. W. Edwards et al., Phys. Rev. **D61** (2000) 072003
25. DELPHI Collab., P. Abreu et al., Eur. Phys. J. **C14** (2000) 585
26. OPAL Collab., P. D. Acton et al., Phys. Lett. **B281** (1992) 405
27. OPAL Collab., R. Akers et al., Z. Phys. **C66** (1995) 31
28. CLEO Collab., R. Balest et al., Phys. Rev. Lett. **75** (1995) 3809
29. OPAL Collab., P. D. Ackerstaff et al., Eur. Phys. J. **C8** (1999) 183
30. CLEO Collab., D. Gibaut et al., Phys. Rev. Lett. **73** (1994) 934